

## Research Paper

# Effect of composition and phase diagram features on printability and microstructure in laser powder bed fusion: Development and comparison of processing maps across alloy systems

Raiyan Seede<sup>a</sup>, Jiahui Ye<sup>b</sup>, Austin Whitt<sup>a</sup>, William Trehern<sup>a</sup>, Alaa Elwany<sup>b</sup>,  
Raymundo Arroyave<sup>a</sup>, Ibrahim Karaman<sup>a,\*</sup>

<sup>a</sup> Department of Materials Science and Engineering, Texas A&M University, College Station, 77843 TX, USA

<sup>b</sup> Wm Michael Barnes '64 Department of Industrial and Systems Engineering, Texas A&M University, College Station, 77843 TX, USA



## ARTICLE INFO

## Keywords:

Printability Maps  
Laser Powder Bed Fusion  
Additive Manufacturing  
Nickel Alloys  
Microsegregation  
Process Optimization

## ABSTRACT

Additive manufacturing (AM) has gained considerable academic and industrial interest due to its ability to produce parts with complex geometries with the potential for local microstructural control. However, due to the large number of material and process variables associated with AM, optimization of alloying compositions and process parameters to achieve desired properties is an arduous task. There is a fundamental gap in understanding how changes in process variables and alloy composition and thermodynamics affect additively manufactured parts. The present systematic study sheds light on the effects of alloying composition and corresponding phase diagram features on the printability and solidification microstructures of four binary nickel-based alloys, namely, Ni-20 at% Cu, Ni-5 at% Al, Ni-5 at% Zr, and Ni-8.8 at% Zr. These compositions are selected to represent binary isomorphous, weak solute partitioning, strong solute partitioning, and eutectic alloying conditions, respectively. Single track and bulk experiments are conducted to quantify the effects of varying material thermodynamic properties such as solidification temperature ranges, alloy melting temperatures, and other solidification conditions on resultant microstructures across the laser powder bed fusion (L-PBF) parameter space. A simple framework for developing processing maps detailing porosity formation and microsegregation across the laser power – scan speed parameter space is established and validated for each of these alloys to determine how material properties affect printability and microstructure in L-PBF. This knowledge will be vital in optimizing alloy chemistry and process parameters to design alloys specifically for additive manufacturing, as well as to provide a path toward local microstructure control.

## 1. Introduction

Laser powder bed fusion (L-PBF) is an additive manufacturing (AM) process with the ability to manufacture metallic parts with complex geometries that would be challenging or impossible to produce with traditional manufacturing techniques. L-PBF has been used to fabricate a variety of alloy systems originally designed for traditional manufacturing processes such as nickel-based super alloys [1–5], Al-Si-Mg alloys [2,6,7], austenitic steels [2,8], Ti-6Al-4V [2,9,10], as well as many other alloys [11–14].

Alloy systems historically used in L-PBF vary widely in both the ranges of manufacturing process parameters required to build fully dense parts as well as their microstructural responses to L-PBF

processing. Nickel-based superalloys such as Inconel 718®, for example, can display cellular-dendritic microsegregation that results from the high cooling rates during solidification associated with L-PBF [2,5,15,16]. On the other hand, Ti-6Al-4V does not typically display microsegregation structures in the as-fabricated condition [17]. Differences in microsegregation between alloys have typically been attributed to the solidification ranges and partition coefficients of the alloys being processed [2], though these discrepancies have not been sufficiently quantified for AM.

Microsegregation can have an impact on the mechanical properties and performance of fabricated parts. In nickel-based superalloys, microsegregation of niobium can lead to the growth of  $\delta$  and laves phases which are detrimental to the performance of these alloys [1,2,5,

\* Corresponding author.

E-mail address: [ikaraman@tamu.edu](mailto:ikaraman@tamu.edu) (I. Karaman).

<https://doi.org/10.1016/j.addma.2021.102258>

Received 25 April 2021; Received in revised form 12 August 2021; Accepted 16 August 2021

Available online 18 August 2021

2214-8604/© 2021 Elsevier B.V. All rights reserved.

15]. Mitigation of these issues has generally consisted of identifying optimized process parameters that circumvent the formation of microsegregation structures [14,18], or implementing post processing homogenization heat treatments [1,2,5,15,19,20]. However, post processing treatments can result in coarse grain structures, and may not be able to resolve the formation of detrimental phases that are stable at high temperatures such as  $\delta$  phase and MC carbides in nickel-based superalloys [5,15]. Therefore, the ideal strategies for mitigating the formation of such detrimental phases are preventing microsegregation by using optimized process parameters or by tailoring alloy composition.

In addition to differences between alloy systems, the selection of process parameters can also have a significant impact on microstructural development [2,14,21]. Using a laser rapid directional solidification model, Liang et al. [21] predicted an increase in the microsegregation of tungsten at low scan speeds and high laser powers in the single crystalline nickel-based super alloy SRR99. Karayagiz et al. [14] developed a framework coupling a finite element thermal model with a non-equilibrium phase field model in order to accurately predict microsegregation in single track scans of an L-PBF fabricated Ni-Nb alloy. They found that cellular-dendritic growth structures varied in both size and solute segregation depending on the linear energy density used for each laser scan [14]. Cellular structures with Nb-rich boundaries were observed at high energy densities, whereas planar growth was shown to dominate the microstructures of low energy density Ni-Nb single tracks [14]. However, these predictions target single laser scans due to the complex thermal histories associated with the layer-by-layer development of L-PBF which can be difficult and computationally expensive to model. Additionally, current literature has focused on predicting microstructural evolution as a function of interface growth velocities (R) and thermal gradients (G), which do not easily translate to usable input parameters for the L-PBF process such as laser power and scan speed [14,22–24]. The establishment of a simple approach to evaluate bulk solidification microstructures across the L-PBF parameter space is therefore highly valuable.

In order to construct processing maps and establish the relationships between L-PBF process parameters and solidification microstructures, a range of parameters that result in full part densification must first be established. Selection of process parameters has a significant impact on the density of AM parts. The mechanisms for porosity formation during AM are well understood [2,25–27], but mitigation strategies are still in the developmental stages. In the past, parameter optimization for fabrication of high density parts was achieved by printing bulk parts in a broad sweep of the parameter space [28–31]. More recently, several approaches have been proposed that utilize predictions of melt pool dimensions to reduce the experimental trials for determining parameters that promote full part density [10,26,27,32–34]. Seede et al. [27] combined an analytical model calibrated with single track experiments and a geometry-based hatch spacing equation in order to build processing maps including three critical L-PBF parameters: laser power, laser scan speed, and hatch spacing. These processing maps were demonstrated to consist of optimal parameter ranges for the production of fully dense parts of a newly developed low alloy steel with a high degree of success [27]. This framework has been validated in-full or in-part for several different alloy systems including steels, Ni-based alloys, and shape memory alloys [27,35–38]. Further development of these processing maps to include a solidification microstructure component would provide a direct link between processing parameters and developed microstructures during LPBF, and allow for both the optimization of microstructure in additively manufactured parts, and the ability to compare printability and microstructure across various alloying compositions in a systematic manner.

There is substantial interest in designing new alloys to address the complex challenges posed by additive manufacturing [39]. In order to develop new alloys, an understanding of how compositional and material property changes affect additively manufactured parts is critical.

The present work utilizes a parameter optimization framework [27] combined with experimental single track microsegregation data in order to develop processing maps for both densification and microstructure in L-PBF. Processing maps are then developed for four binary nickel-based alloys, namely, Ni-20 at% Cu, Ni-5 at% Al, Ni-5 at% Zr, and Ni-8.8 at% Zr in order to represent binary isomorphous, weak solute partitioning, strong solute partitioning, and eutectic alloying conditions, respectively. Quantitative wavelength dispersive spectroscopy (WDS) observations of both single track and bulk experiments are used to validate the processing maps as well as to elucidate the effects of material properties and alloying conditions on printability and microstructure in L-PBF. An empirical model is developed by exploiting the dataset generated in this study using machine learning approaches to accurately predict dendritic microsegregation structures as a function of L-PBF process parameters and easily accessible material property inputs.

## 2. Experimental methodology

### 2.1. Alloy selection

There are currently no generally recognized criteria for the development or selection of alloy systems tailored to AM. However, insight can be gained from welding literature and studies on rapid solidification [40]. A key challenge is posed by microsegregation from dendritic solidification which can cause solidification cracking and undesirable phase formation in AM. This phenomenon depends on the speed of the solidification front and the equilibrium partition coefficient ( $k_e$ ). The equilibrium partition coefficient is the ratio of solid and liquid solute concentrations in an alloy system ( $k_e = C_s/C_l$ ). Under non-equilibrium rapid solidification conditions, such as those typical in L-PBF, the partition coefficient is velocity dependent [41]. This indicates that an increase of solidification speed through the increase in laser scan speed is expected to reduce microsegregation, as has been demonstrated in the literature [14]. However, it may not be feasible to process certain alloys at high enough speeds to completely resolve dendritic solidification. When designing alloys for AM, the equilibrium partition coefficient can be utilized to control microsegregation. An alloy with a  $k_e \approx 1$  may not require high printing speeds as microsegregation is not expected to occur. It may therefore be possible to use simple equilibrium phase diagram features to select potential alloy systems that would not exhibit solute trapping. Similarly, eutectic alloys solidify into two solid phases without passing through a liquid plus solid region which would circumvent microsegregation. The coupled phases that grow during eutectic solidification become more refined with increasing cooling rate, and often display excellent mechanical properties [42,43]. The microstructural complexity and the differences in alloy compositions of multicomponent commercial alloys can make generalized analysis of printability across alloy systems difficult. For these reasons, the following four binary alloys are selected as simple model alloy systems for L-PBF processing to assess the role of alloy composition, phase diagram features, and material physical properties in printability and microstructure evolution during AM. Binary phase diagrams for these alloys are displayed in Fig. 1 [44–46], and relevant material properties calculated using CALPHAD Thermo-Calc software [47] can be found in Table 1.

- **Ni-20 at% Cu:** A Ni-Cu alloy is selected due to its fully isomorphous system. This alloy is expected to exhibit microsegregation due to its non-unity partition coefficient ( $k_e = 0.74$ ) and moderate solidification range (20 K). The lack of secondary phase formation during solidification in this alloy will serve to contrast with microstructural development in the multi-phase alloy systems selected below.
- **Ni-5 at% Al and Ni-5 at% Zr:** In order to investigate the effect of an alloy's partition coefficient on the homogeneity of AM microstructures, two nickel-based alloys with equivalent binary composition Ni<sub>95</sub>X<sub>5</sub> (at%), where X is the solute element, are selected. The Ni-Al

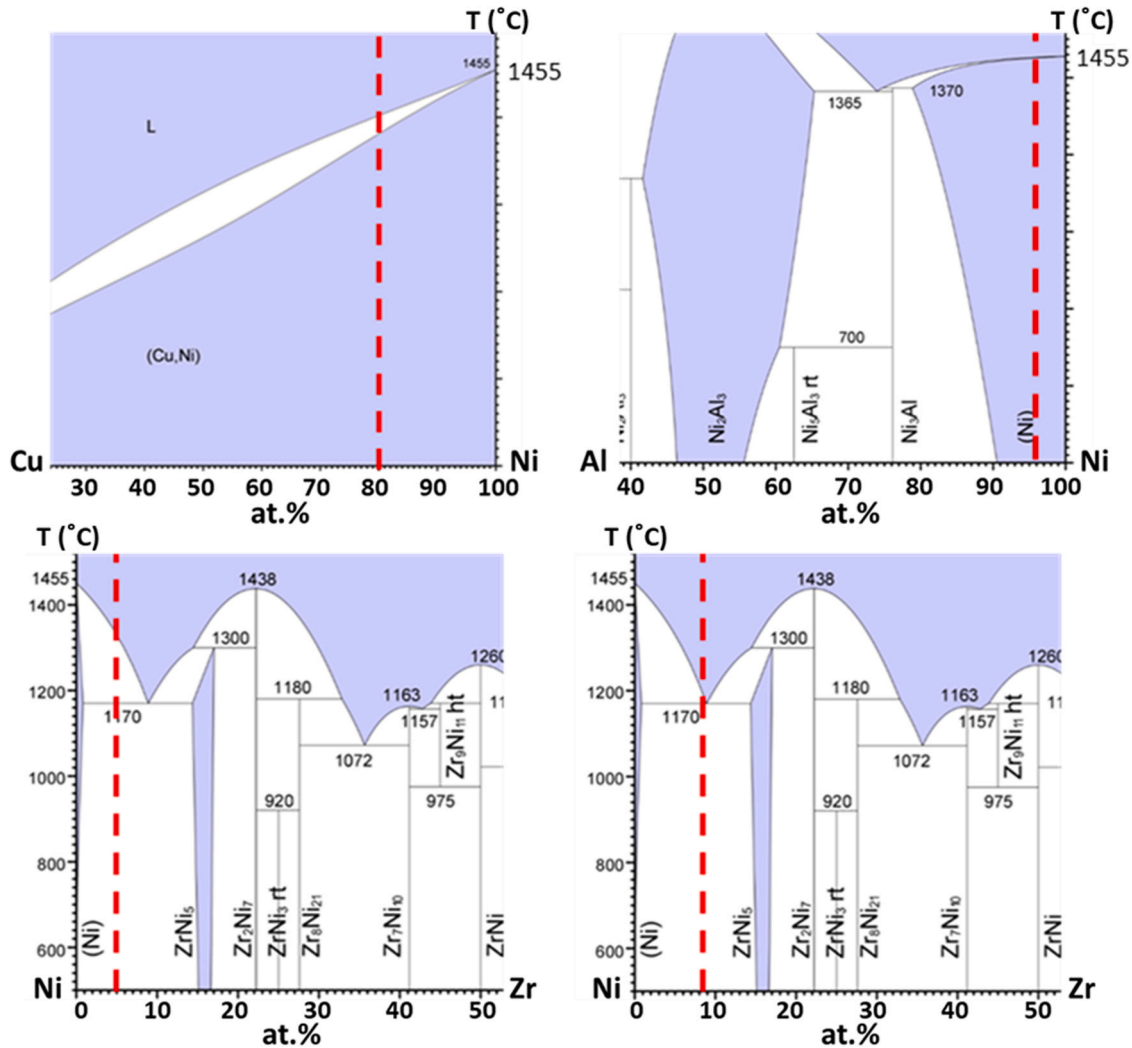


Fig. 1. Binary phase diagrams of the four alloys used in this study: Ni-20 at% Cu, Ni-5 at% Al, Ni-5 at% Zr, and Ni-8.8 at% Zr [44–46]. The dashed red lines indicate the alloy composition within each of the phase diagrams. (For interpretation of the references to color in this figure legend, the reader is referred to the web version of this article.)

Table 1

Material properties of the four alloys used in this study: Ni-20 at% Cu, Ni-5 at% Al, Ni-5 at% Zr, and Ni-8.8 at% Zr. The values in this table were calculated using CALPHAD Thermo-Calc software [47].

Alloys (at %)	Solidification Range ( $\Delta T$ )	Partition Coefficient ( $k_e$ )	Melting Temperature ( $^{\circ}C$ )
Ni-20 at% Cu	20	0.74	1377
Ni-5 at% Al	0.2	0.96	1417
Ni-5 at% Zr	172	0.11	1327
Ni-8.8 at% Zr	0	1	1167

and Ni-Zr systems are ideal for testing partition coefficient effects due to the significant difference in solute partitioning. Ni-5 at% Al is expected to display little to no microsegregation as its liquidus and solidus are nearly identical for all temperatures and its  $k_e = 0.96$ . However, significant microsegregation is expected in the Ni-5 at% Zr alloy due to the large freezing range (172 K) and low partition coefficient ( $k_e = 0.11$ ).

- Ni-8.8 at% Zr:** This composition of the Ni-Zr system is selected in order to study and contrast the effects of L-PBF processing conditions on a eutectic alloy in comparison with the previously selected alloys. Eutectic alloys exhibit coupled growth between two phases that exchange mass ahead of the solidification front. Under very rapid solidification conditions, microstructural formation can become dominated by nucleation of the uncoupled solid phases. This effect is termed anomalous growth and is due to solidification time scales becoming too short for effective diffusion to occur ahead of the solidification front [48,49]. If this does not occur, microsegregation is not expected to be observed in the eutectic alloy. Instead, a fine lamellar structure may be expected due to the high cooling rates characteristic of the L-PBF process [2].

## 2.2. Process parameter optimization

In order to determine a region in the laser power-scan speed parameter space that circumvents porosity formation for each of the four alloys, a parameter optimization framework proposed by Seede et al. [27] is implemented. This framework uses the computationally inexpensive Eagar-Tsai (E-T) [50] analytical thermal model to provide low fidelity predictions of melt pool dimensions across the parameter space. These initial predictions are then used to sample the laser power-scan

speed space with single track experiments to conduct statistical calibration of the model for higher fidelity predictions. For this purpose, 46 single track experiments were sampled with a grid-based sampling strategy throughout the parameter space and are displayed as markers on the plots in Fig. 2. Boundaries of the laser power ( $P$ ) – scan speed ( $v$ ) sampling space were selected as  $(P_{\min}, P_{\max}) = \{71, 260 \text{ W}\}$  and  $(v_{\min}, v_{\max}) = \{0.05, 2.5 \text{ m/s}\}$ . Values for  $P_{\max}$  and  $v_{\max}$  were set to the machine limitations, and  $v_{\min}$  was selected to avoid prohibitively slow scan speeds.  $P_{\min}$  was selected as the lowest power necessary to attain a melt pool depth equal to one layer thickness at  $v_{\min}$  in the alloy with the largest melting temperature (Ni-5 at% Al) as predicted by the E-T model. The parameter space was then split into two regions for grid-based single track sampling. Thirty single tracks were sampled between  $v_{\min} = 0.05 \text{ m/s}$  and  $v = 1.3 \text{ m/s}$ , and the remaining 16 single tracks were sampled between  $v = 1.3 \text{ m/s}$  and  $v_{\max} = 2.5 \text{ m/s}$ . The first region was sampled more densely as it is expected to contain most of the optimal printability regions for all alloy systems. Keyholing and balling single tracks were classified qualitatively from top-view and cross sectional micrographs based on the characteristic features of these defect mechanisms [2,26,27,51,52]. Previous studies have classified lack of fusion single tracks using a melt pool depth = layer thickness criteria [26,27,35]. However, Zhang et al. [35] reported that high density prints can

still be achieved within this lack of fusion region, demonstrating the need to relax this constraint. Since a single track lack of fusion criterion is somewhat arbitrary due to the necessity of printing multiple single tracks and at least few layers to form lack of fusion porosity, a less conservative value is selected to expand the functional printability region. Lack of fusion single tracks were classified based on the experimental measurements and a criterion of melt pool depth  $\leq 0.667 \times$  layer thickness ( $D \leq 0.667 t$ ). This value is selected as the minimum single track depth required to penetrate the solid printed substrate after 10 layers, based on the assumptions that the effective height of a layer printed on the substrate is equal to the powder packing density  $\times$  the layer thickness and that the relative powder packing density is  $\sim 60\%$ .

A statistical methodology based on the Kennedy and O'Hagan [53] calibration framework is then implemented in two steps. The first step consists of constructing a surrogate model using Gaussian process regression which is combined with the measured melt pool dimensions for calibration. The next step utilizes a discrepancy function to account for model inadequacies to ensure accuracy between the calibrated model predictions and the experimental measurements. Melt pool dimension predictions from the fully calibrated model are then used to establish the lack of fusion and keyholing boundaries displayed in Fig. 2.

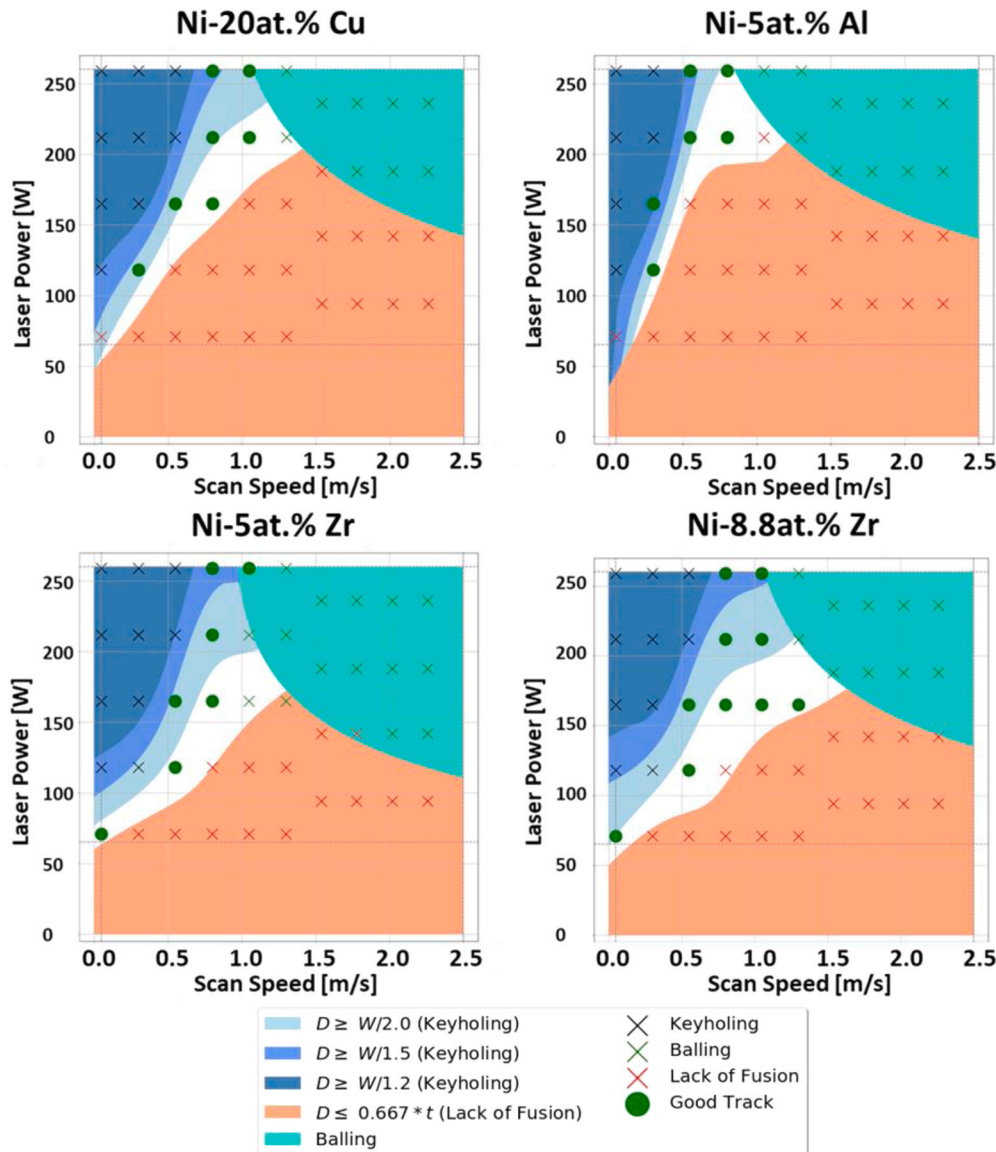


Fig. 2. L-PBF process parameter maps are displayed for Ni-20 at% Cu, Ni-5 at% Al, Ni-5 at% Zr, and Ni-8.8 at% Zr. These maps contain various keyholing criteria ( $W/D \leq 1.2, 1.5, 2.0$ ) to determine which criterion fits best, and a lack of fusion criterion ( $D \leq 0.667 t$ ), predicted by the calibrated Eagar – Tsai (ET) model discussed in Section 2.2. A balling region fit to single track experiments using a Support Vector Machine (SVM) classifier is also plotted. Experimentally classified single-tracks exhibiting keyholing, lack of fusion, balling, and good track characteristics are marked with different symbols and colors in these maps demonstrating a good match with ET model predictions.  $D$ : Melt Pool Depth,  $W$ : Melt Pool Width,  $t$ : Powder Layer Thickness. (For interpretation of the references to color in this figure legend, the reader is referred to the web version of this article.)

Potential defect boundaries are selected based on melt pool dimension relationships that have been observed to correspond well with defect formation, namely, a melt pool width/depth relationship ( $W/D$ ) to determine keyholing and a melt pool depth/layer thickness ( $D/t$ ) relationship to determine lack of fusion boundaries [26,27,32,54,55]. Several keyhole criteria are plotted and compared to experimentally characterized single tracks in Fig. 2 to visualize which boundary best fits each material based on the experimental observations. The keyholing criteria selected for comparison were chosen based on values established in the literature ( $W/D \leq 1.2, 1.5, 2.0$ ) [27], and the lack of fusion criterion was selected as  $D/t \leq 0.667$ . A defect boundary for balling was established using a support vector machine classifier (SVM) [56] that uses experimental single track classifications to divide the processing map into balling and non-balling regions. A 3rd degree polynomial kernel SVM classifier [57] was used to determine the balling region of each material. Once these defect criteria are established, finalized processing maps can be created for each alloy. It should be noted that the methodology described for building processing maps in this work is intended to be AM machine specific, as single tracks built in different machines may display differences in melt pool morphologies.

To ensure proper fusion between melt pools, a geometrically-based hatch spacing criterion is implemented [27]. This criterion was

derived under the conservative assumption that the transverse shape of each melt pool is parabolic both above and below the printing surface. Melt pool height is also assumed to be equal to the layer thickness due to the difficulty of predicting melt pool height. The criterion states that the maximum value of hatch spacing ( $h_{max}$ ) that can be used before voids form between two melt pools in two successive tracks follows the equation:

$$h_{max} = W \sqrt{1 - \frac{t}{t+D}} \tag{1}$$

where  $W$  is the width of a melt pool,  $D$  is the depth of a melt pool, and  $t$  is the layer thickness. This equation allows for the determination of a maximum hatch spacing boundary at any point in the parameter space based only on melt pool dimensions and layer thickness. This equation was used to plot maximum hatch spacing contours on finalized processing maps for each alloy, as displayed in Fig. 3. Three parameter sets were selected from each alloy at different locations in the parameter space to print  $8 \times 8 \times 8$  mm cubes based on the processing maps in Fig. 3. Hatch spacing values selected to print the cubes were rounded down to the nearest multiple of five. The parameters chosen for each of these cubes is listed in Table 2.

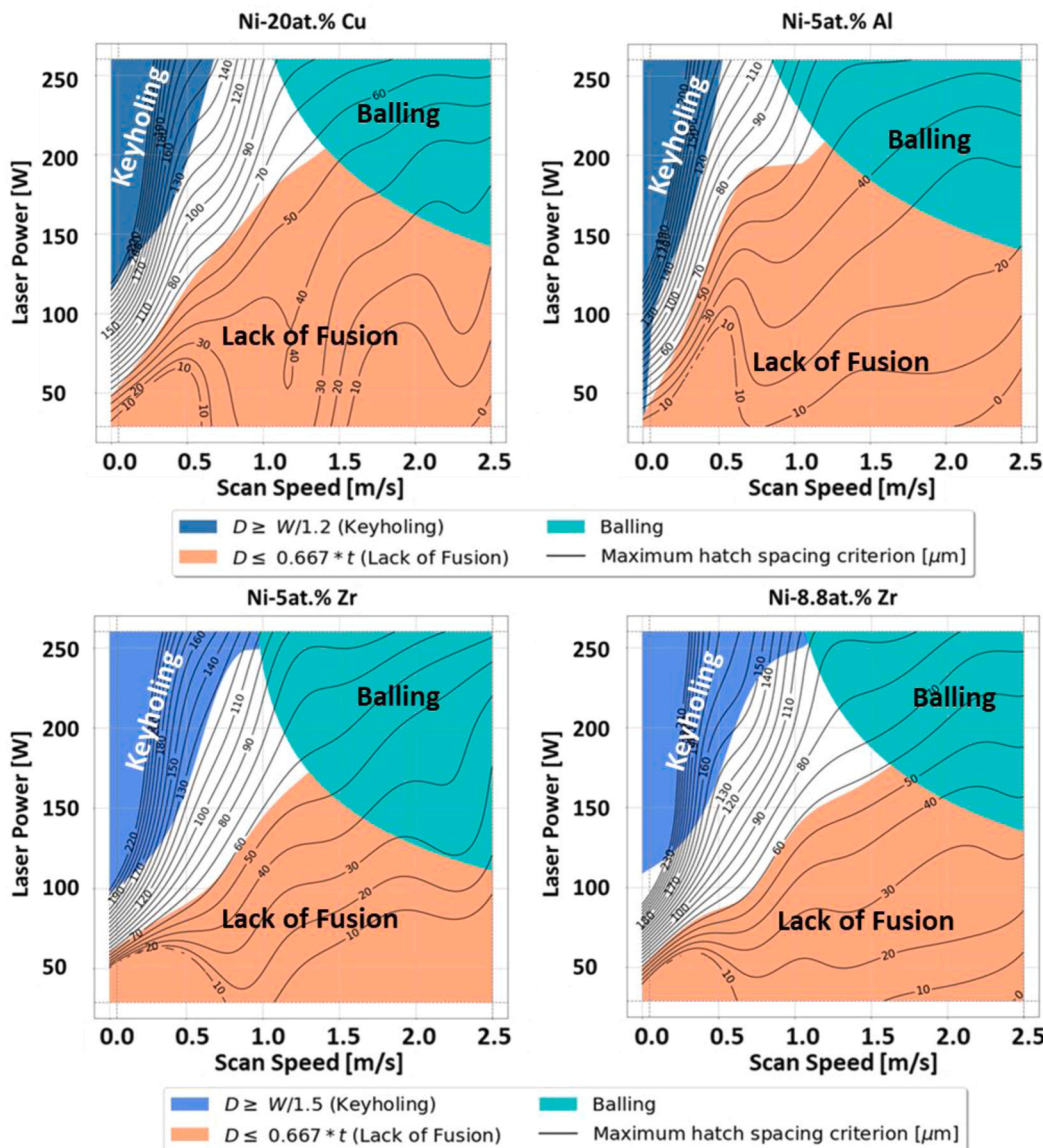


Fig. 3. L-PBF process parameter maps with finalized selections of keyholing criteria and maximum hatch spacing contours. The keyholing criterion selected for Ni-20 at % Cu and Ni-5 at% Al is  $W/D \leq 1.2$ , and  $W/D \leq 1.5$  for Ni-5 at% Zr and Ni-8.8 at% Zr. Lack of fusion criteria is kept at  $D \leq 0.667t$  for all maps, and the balling region was fit to single track experimental data using a Support Vector Machine (SVM) classifier.  $D$ : Melt Pool Depth,  $W$ : Melt Pool Width,  $t$ : Powder Layer Thickness,  $h_{max}$ : Maximum Hatch Spacing.

**Table 2**

A list of the processing parameters selected to print  $8 \times 8 \times 8$  mm cubes within the optimal process parameter regions of the processing maps in Fig. 3.

Alloy Composition	Laser Power (W)	Scan Speed (m/s)	Hatch Spacing ( $\mu\text{m}$ )	Layer Thickness ( $\mu\text{m}$ )
Ni-20 at% Cu	115	0.05	200	49
	120	0.30	110	
	225	0.90	100	
Ni-5 at% Al	100	0.05	130	
	125	0.30	85	
	240	0.90	85	
Ni-5 at% Zr	75	0.05	120	
	110	0.30	125	
	140	0.90	60	
Ni-8.8 at% Zr	80	0.05	165	
	120	0.30	160	
	130	0.90	60	

### 2.3. Microsegregation processing maps

The calibration framework outlined in Section 2.2 provides processing maps detailing porosity formation regions in the L-PBF parameter space. However, these maps do not provide information detailing changes in microstructural features across the parameter space. One difficulty in characterizing microstructural feature differences is the quantification of these features. Microsegregation of solute elements can be measured using energy dispersive (EDS) or wavelength dispersive spectroscopy (WDS), however, generating this data for a large number of samples is preventatively costly and time consuming. Primary dendrite arm spacing (PDAS) in microsegregation structures has been demonstrated to be dependent on both laser power and scan speed in L-PBF [14]. However, PDAS can vary significantly at different locations within a single melt pool [14]. It is therefore crucial to note that PDAS is used as a convenient quantifiable value with the intent of qualitatively mapping microsegregation across the parameter space. PDAS values measured in single tracks will likely not be representative of PDAS values in bulk parts. However, a decreasing trend in PDAS values within the parameter space is expected to indicate a decrease in overall microsegregation within a part. In order to map microsegregation in each alloy across the laser power-scan speed parameter space, PDAS is measured in each of the 46 single tracks printed for all four alloy systems. Interpolation over the laser power-scan speed parameter space is then conducted on the PDAS dataset via multilevel B-splines approximation using the R function *mba.surf* in the *MBA* package [58] in order to generate heat maps based PDAS values in the laser power-scan speed parameter space. Observations of planar growth instead of cellular-dendritic growth structures are indicated by zero values in the heat map. These maps are validated by WDS composition maps of the single tracks and cubes. Lastly, the heat maps are combined with the porosity-free processing maps to detail a processing region that will result in full density parts with desired microstructural outcomes.

### 2.4. Materials fabrication and characterization

Gas atomized Ni-5 at% Al, Ni-20 at% Cu, Ni-5 at% Zr, and Ni-8.8 at% Zr powder provided by Nanoval GmbH & Co. KG were used to manufacture L-PBF single tracks and cubes. These specimens were printed using a 3D Systems ProX DMP 200 commercial L-PBF system (fiber laser with a Gaussian profile  $\lambda = 1070$  nm, and nominal beam diameter =  $80 \mu\text{m}$ ).

Single tracks were printed on a base plate of the same composition as each respective alloy. Base plates were all procured in the as-cast condition. The Ni-5 at% Al as-cast base plate was subjected to homogenization at  $1100^\circ\text{C}$  for 1 h, 50% cold rolling, and recrystallization at  $700^\circ\text{C}$  for 1 h. The Ni-20 at% Cu as-cast base plate was subjected to homogenization at  $1100^\circ\text{C}$  for 1 h, 50% cold rolling, and recrystallization at  $800^\circ\text{C}$  for 1 h. The Ni-5 at% Zr as-cast base plate was subjected

to homogenization at  $1000^\circ\text{C}$  for 1 h and 38% hot rolling at  $850^\circ\text{C}$ . The Ni-8.8 at% Zr as-cast base plate was subjected to homogenization at  $850^\circ\text{C}$  for 1 h and 12.6% hot rolling at  $800^\circ\text{C}$ . Single tracks were 10 mm in length with 1 mm spacing between tracks, and each material was printed at the same 46 combinations of laser power and scan speed with a constant powder layer thickness of  $49 \mu\text{m}$ , which roughly corresponds to the d80 of the powders (the 80th percentile of the powder size distribution). Cross sections of the single tracks were cut using wire electrical discharge machining (EDM), and these specimens were polished down to  $0.25 \mu\text{m}$  with water-based diamond suspension polishing solutions, and vibratory polished with  $0.04 \mu\text{m}$  colloidal silica for 2 h. Kalling's Solution No. 2 (5 g  $\text{CuCl}_2$ , 100 mL HCl, and 100 mL ethanol) was used to etch the single tracks to obtain optical and backscattered electron micrographs. Melt pool dimensions were taken from the average values measured in cross sectional images of each single track at three locations. Primary dendrite arm spacing (PDAS) was imaged using backscattered electron micrographs of the single track cross sections in the as-etched condition. At least 20 PDAS measurements were made at the melt pool edge of each single track. Three cross sections of each single track were used for analysis of PDAS to ensure that the observations were representative of the entire melt pool. Single tracks displaying planar growth were marked as having a PDAS of  $0 \mu\text{m}$ . Square cubes ( $8 \times 8 \times 8$  mm) were printed using the process parameters listed in Table 2 for microstructural analysis.

Optical microscopy (OM) was carried out using a Keyence VH-X digital microscope equipped with a VH-Z100 wide range zoom lens. Wavelength dispersive spectroscopy (WDS) was performed with a CAMECA SXFive electron probe microanalyzer equipped with a  $\text{LaB}_6$  electron source. Quantitative WDS composition maps were obtained at settings of 15 kV, 50 nA, and  $110 \mu\text{s}$  pixel dwell time with a  $0.1 \mu\text{m}$  step size. WDS was carried out on specimens in the as-polished condition, and WDS maps are displayed in atomic% (at%). Backscattered electron images were taken using a FEI Quanta 600 SEM equipped with a field emission electron source.

## 3. Results and discussion

### 3.1. Powder characterization

Surface morphology and cross sectional microstructure of the gas atomized Ni-5 at% Al (NiAl), Ni-20 at% Cu (NiCu), Ni-5 at% Zr (Ni-5Zr), and Ni-8.8 at% Zr (Ni-8.8Zr) powders are displayed in Fig. 4. Micro-dendritic features are directly observable on the surfaces of the NiCu and Ni-5Zr powder particles. Grain boundaries are similarly observed on the surfaces of the NiCu and NiAl powder. Cross sections of the Ni-5Zr powder revealed white segregation structures, whereas grain structures are observed in the NiCu and NiAl cross sections. NiCu powder particles may contain Cu segregation, however, the similarity in atomic number between Ni and Cu may result in poor contrast in the back-scattered electron micrograph between regions of Cu segregation and the matrix. The Ni-8.8Zr eutectic powder displays a fine lamellar microstructure characteristic of eutectic alloys subjected to high solidification rates [42,43]. These results indicate the dependence of solidification microstructures on the solidification range of each alloy. The clear microsegregation observed in Ni-5Zr is likely due to the large solidification range and low  $k_e$  of the alloy (172 K and 0.11, respectively). On the other hand, no segregation of Al is present in the NiAl alloy due to its small freezing range and  $k_e$  value (0.2 K and 0.96, respectively). The larger freezing range allows time for solute rejection from the matrix phase during solidification. This results in the observed cellular-dendritic structures in the powder particles.

### 3.2. Comparing single track dimensions and printability across alloy systems

Two laser heating modes influence melt pool geometry: conduction

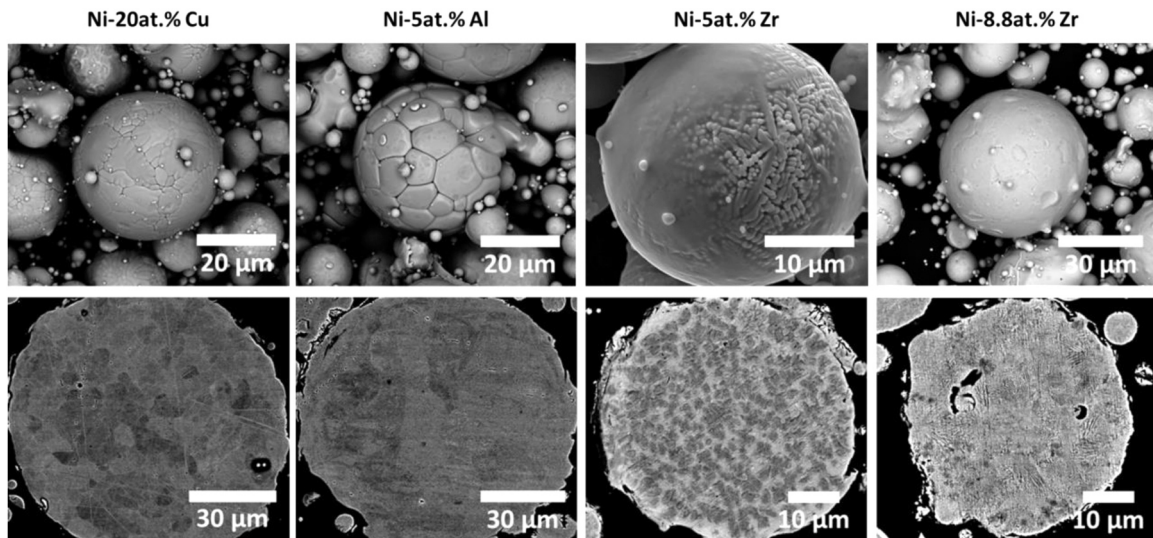


Fig. 4. Scanning electron microscope images of gas atomized Ni-20 at% Cu, Ni-5 at% Al, Ni-5 at% Zr, and Ni-8.8 at% Zr powder particle morphology is displayed in the first row of micrographs and cross sections of these particles are displayed in the second row of micrographs.

mode and keyhole mode heating. Conduction mode melting occurs at low energy densities and is characterized by a wide and shallow melt pool, whereas keyholing occurs at high energy densities and is charac-

terized by deep melt pools. The optical micrographs in Fig. 5 reveal a clear trend from conduction to keyhole mode heating as the linear energy density ( $LED = \frac{P}{v}$ ) increases from left to right in each alloy (147.5 J/

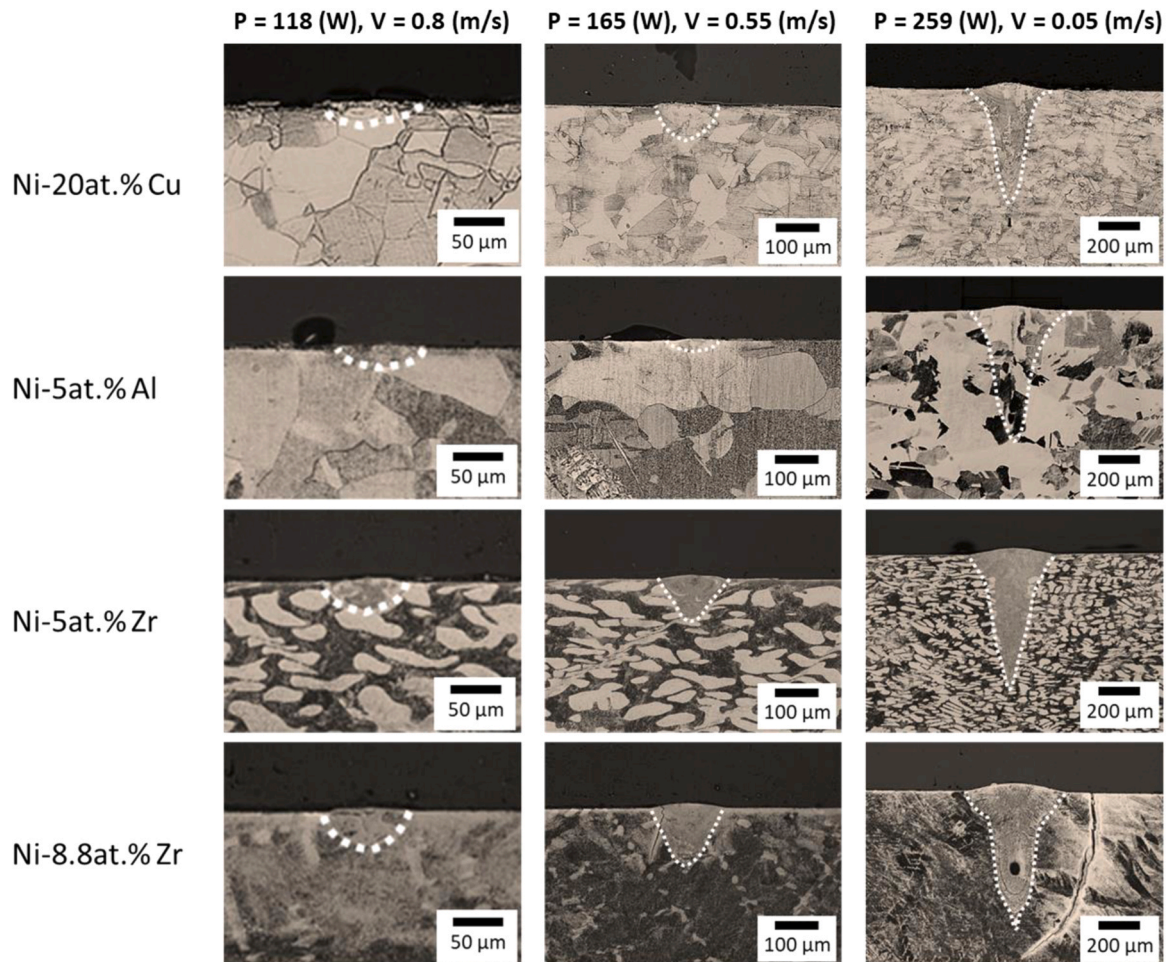


Fig. 5. Optical micrographs of cross sections of single tracks printed at three different parameter sets for each of the alloys printed in this study:  $P$ : 118 W,  $v$ : 0.8 m/s;  $P$ : 165 W,  $v$ : 0.55 m/s; and  $P$ : 259 W,  $v$ : 0.05 m/s. White dotted lines indicate the boundaries of single tracks that are difficult to distinguish in these images. These single tracks demonstrate a transition between conduction mode heating and keyholing in L-PBF.

m, 300 J/m, 5180 J/m respectively). The contrast between single tracks printed at the same parameters is easily observed in Fig. 5, and a correlation between alloy liquidus temperature and melt pool dimensions can be seen. NiAl has the highest melting temperature (1417 °C) of the four alloys and appears to have the smallest melt pools at each parameter set. In comparison, Ni-8.8Zr displays the largest observable melt pools and has the lowest melting temperature (1167 °C). At the LED of 300 J/m, NiCu, Ni-5Zr, and Ni-8.8Zr show mixed conduction – keyhole mode melting whereas NiAl displays a melt pool morphology indicative of conduction mode melting. This relationship between melt pool dimensions and alloy melting temperature is more clearly demonstrated in Fig. 6, which displays distinct trends in melt pool width (Fig. 6a) and depth (Fig. 6b) for each material. Both the width and depth of the single tracks appear to be dependent on the melting temperature of each alloy. For both width and depth, the order of materials from smallest to largest melt pools and highest to lowest melting temperatures is: NiAl (1417 °C), NiCu (1377 °C), Ni-5Zr (1327 °C), and Ni-8.8Zr (1167 °C). These results are intuitive, as alloys that require less energy to melt would be expected to undergo more melting when exposed to the same

level of energy. However, it is interesting to note that despite the large difference in melting temperature (up to 285 K for NiAl and Ni-8.8Zr), many of the single tracks are within one standard deviation of each other in both width and depth at each parameter set. The largest differences in melt pool dimensions between alloys occur at LEDs above 1000 J/m.

These melt pool dimension variations can explain the differences in the identified optimal printing region between each alloy's processing map displayed in Fig. 3. NiAl is observed to have the smallest printable region out of the four alloys due to the large lack of fusion region. Since the lack of fusion region criterion is based on predicted melt pool depth, NiAl's higher melting temperature and shallower melt pools result in a larger lack of fusion region compared to the other alloys. The lack of fusion boundaries for all four alloys follow a similar trend as the melt pool dimensions. Alloys with larger melting temperatures display larger lack of fusion regions. However, the opposite appears to be true of keyholing boundaries in these alloys. Ni-5Zr and Ni-8.8Zr display larger keyholing regions compared to the NiCu and NiAl alloys. This is in part due to the difference in keyholing criteria selected for these maps; NiCu

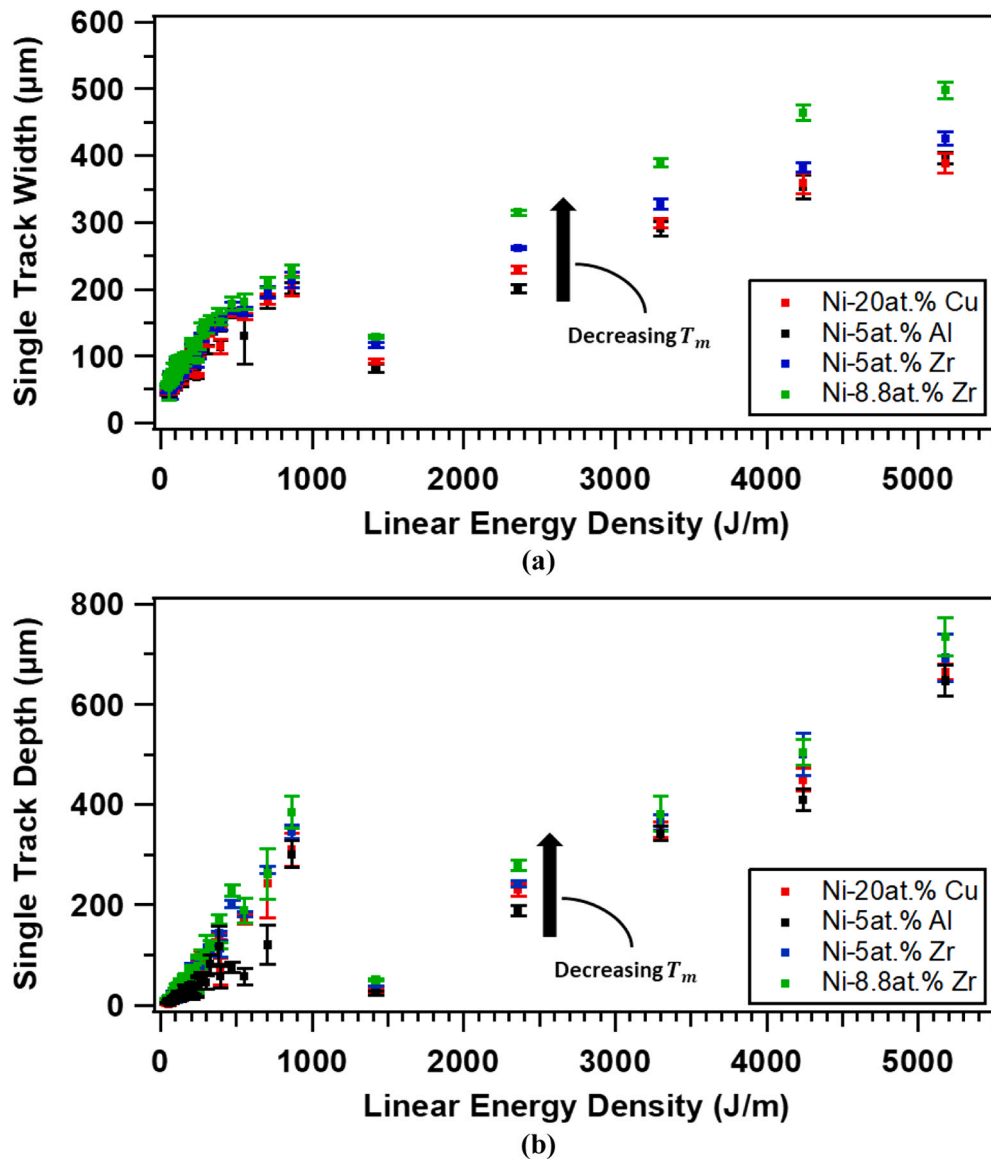


Fig. 6. Plots of measured single-track melt pool dimensions against linear energy density: a) is a plot of the observed single-track widths for each material and b) is a plot of the observed single-track depths for each material. Error bars display 1 standard deviation away from the mean in each direction. The black arrows indicate that alloys displaying larger melt pool dimensions have lower melting temperatures ( $T_m$ ).

and NiAl have a keyholing criterion of  $W/D \leq 1.2$ , whereas Ni-5Zr and Ni-8.8Zr have a keyholing criterion of  $W/D \leq 1.5$ . However, these criteria were selected based on experimental observations of single tracks in these regions. Single tracks in the two Ni-Zr alloys were observed to display keyholing at lower laser powers than those in NiCu and NiAl. This is also likely to be attributable to melting temperature. Lower melting temperatures reduce the energy barrier for melting resulting in deeper melt pools, as is observed in Fig. 6b. It appears that the lack of fusion boundary is more sensitive to this effect than the keyholing boundary, since the printable region for each of the alloys gets larger at lower melting temperatures.

### 3.3. Comparing single track microstructure across alloy systems

Composition analysis of the single tracks at several parameter sets was conducted using quantitative WDS measurements. Fig. 7 displays optical micrographs and WDS maps taken from the largest energy density parameter set ( $P = 259$  W,  $v = 0.05$  m/s, and  $LED = 5180$  J/m) used to print single tracks for each alloy. Fig. 7 displays optical micrographs of the single tracks in the left column with red and blue boxes indicating WDS map locations. The middle column of Fig. 7 shows WDS maps taken from the top of each melt pool, and the right column shows maps taken from the edges of each melt pool. Differences in segregation structure are easily observable in WDS maps at the top of each melt pool. NiCu displays notable cellular structures in both the top and the edge of the melt pool. Up to 5 at% additional segregation of Cu is observed in the WDS map at the top location of the melt pool. NiAl and Ni-8.8Zr display completely homogenous microstructures, showing no compositional

segregation at the top of the melt pools. This is likely due to the small solidification ranges in NiAl and Ni-8.8Zr (0.2 K and 0 K respectively). Even lamellar structures are not observable in WDS maps of the eutectic Ni-8.8Zr alloy. This may be due to the extremely high cooling rates associated with the additive manufacturing process, which may result in nanoscale lamellar solidification too fine to be detected by the instrument. Ni-5Zr displays large dendrite structures at the top of the melt pool. These structures appear to have primary and secondary dendrite arms with up to 6 at% additional segregation of Zr. Large dendrite structures have time to form during solidification of the Ni-5Zr alloy due to the large solidification range of the material (172 K).

Single-track fusion boundaries are observable in the WDS maps taken at the edges of each melt pool (Fig. 7). Around 4 at% Cu depletion is observed at the fusion boundary of the NiCu single track, along with columnar segregation structures inside the melt pool. This Cu depletion is indicative of a transient at the fusion boundary as the solidification grows by accelerating from zero velocity. Low growth rates during solidification can explain the appearance of planar structures near the fusion boundary. Solidification starts at the fusion boundary once the material drops below the liquidus temperature. The planar structure at the fusion boundary transitions to a columnar segregation structure as the temperature drops below the liquidus and the growth rate surpasses the constitutional supercooling limit. The microstructure differs greatly at each location of the melt pool in NiCu, showing cellular segregation at the top and columnar segregation at the edge. This is due to variation in thermal conditions and growth velocities at different locations along the solidification front. However, the cell structures at the top of the NiCu melt pool display similar sizes, which suggests that the cells are in a

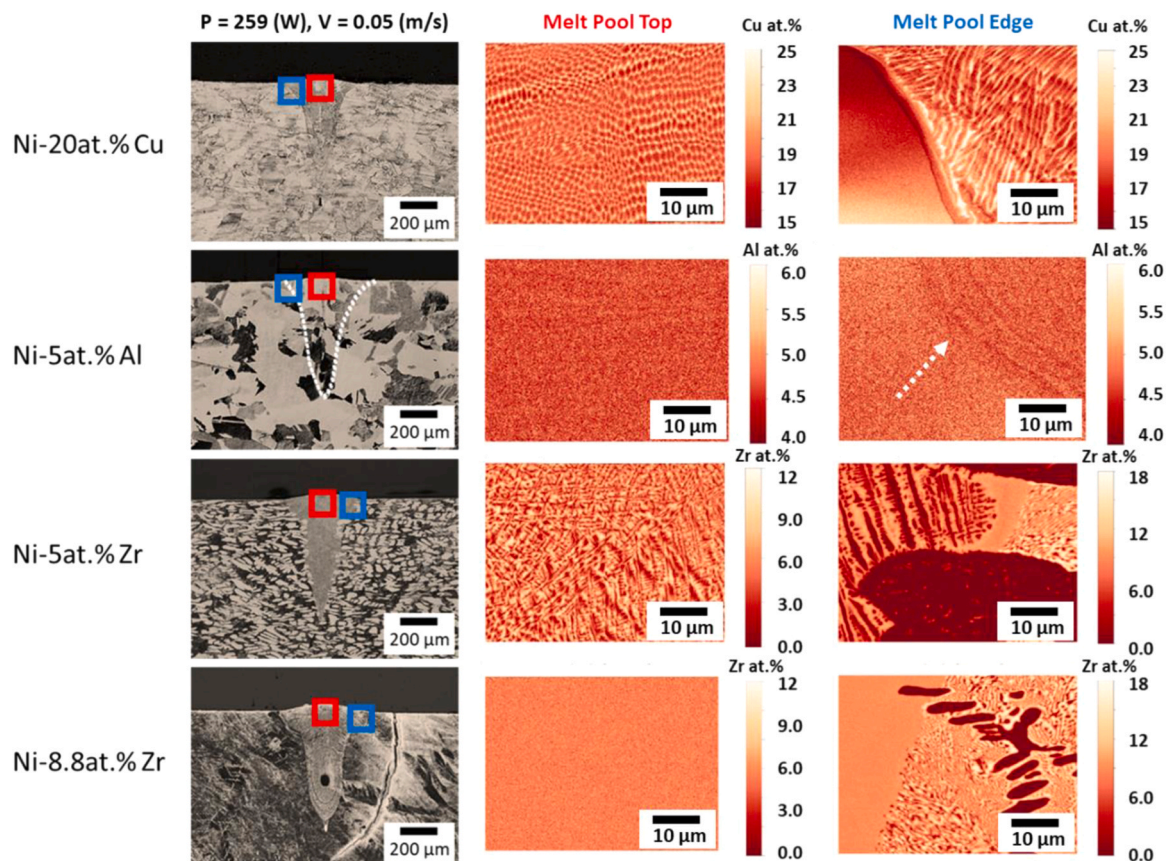


Fig. 7. Optical micrographs of single tracks for each alloying composition printed at 259 W and 0.05 m/s are displayed in the left column with red and blue boxes indicating where WDS maps were conducted. The middle column shows WDS maps taken from the top of each melt pool, and the right column shows maps taken from the edges of each melt pool as color coded in the optical micrographs. White dotted lines indicate the boundaries of single tracks that are difficult to distinguish in these images. The white dotted arrow indicates the edge of the NiAl single track. (For interpretation of the references to color in this figure legend, the reader is referred to the web version of this article.)

steady-state condition at that location. NiAl similarly displays Al depletion at the melt pool boundary. However, the solute Al atoms have far less time to segregate out of the matrix due to the lower solidification range ( $\Delta T$ ) and the effect is much smaller than in NiCu ( $< 1$  at% depletion). Ni-5Zr displays a large homogenous region along the melt pool boundary and Zr depleted dendrite structures inside the melt pool at the edge location. This may indicate the opposite effect of those observed in NiCu and NiAl, where Zr segregates at the melt pool boundary enough to solidify as a eutectic. It is also possible that mixing between the molten pool and the observed local Ni<sub>5</sub>Zr phases in the base plate caused a local increase of Zr during the laser scan. This would explain the compositional homogeneity observed along the melt pool boundary in Ni-5Zr, which is very similar to what is observed at the top of the eutectic Ni-8.8Zr single track. The Ni-8.8Zr alloy displays an immediate transition between the molten pool and the eutectic base plate, with no Zr depletion observed. The complete homogeneity within the Ni-8.8Zr melt pool indicates how critical the freezing range of an alloy is to microstructure in additively manufactured materials.

Figs. 8 and 9 display optical micrographs and WDS maps of single tracks at several parameter sets with lower energy densities than Fig. 7. Cellular microsegregation structures are faintly observable in both the top and edge locations of NiCu printed at  $P = 212$  W,  $v = 0.3$  m/s, and  $LED = 706.7$  J/m. At these parameters, less Cu segregation is observed (up to 3.5 at%) compared to single tracks printed at 5180 J/m (up to 5 at%). No significant features are observed in the NiAl WDS maps in Fig. 8, indicating that solidification speeds at these parameters are too high for even solute depletion at the melt pool boundary. Similarly to NiCu, Ni-5Zr displays lower relative amounts of segregation (up to 4 at% Zr) compared to tracks printed at 5180 J/m (up to 6 at%). Ni-8.8Zr does

not show significant differences in microstructure between the tracks printed at 706.7 J/m and 5180 J/m, displaying complete compositional homogeneity at both parameter sets. Fig. 9 shows single tracks printed at two parameter sets ( $\{P = 165$  W,  $v = 0.55$  m/s,  $LED = 300$  J/m}, and  $\{P = 118$  W,  $v = 0.8$  m/s,  $LED = 147.5$  J/m}). NiCu, NiAl, and Ni-8.8Zr display planar microstructures at both parameter sets. Compositional fluctuation is observed in the WDS maps of NiCu, which may be due to local compositional differences in the baseplate and mixing between the base plate and the deposited powder. Ni-5Zr displays faint dendrite structures in the single track printed at 300 J/m, however, a planar structure is observed at 147.5 J/m. Variations in composition for Ni-5Zr printed at 147.5 J/m can be similarly attributed to local compositional differences between the powder and baseplate.

#### 3.4. Printability-microstructure processing maps and cube sample validation

PDAS is measured for each of the 46 single tracks across the four alloy systems to map the evolution of microsegregation across the laser power – scan speed parameter space. Fig. 10 displays backscattered electron micrographs of etched NiCu single track cross sections that exemplify changes in PDAS at four different parameter sets. These micrographs demonstrate significant increases in dendrite size with increasing energy density. This is due to the changes in temperature gradient ( $G$ ) and growth rate ( $R$ ) with changing process parameters. Decreasing heat input results in smaller molten pools and a higher cooling rate ( $G \times R$ ), whereas increasing heat input results in larger molten pools and lower cooling rates [23]. Lower relative cooling rates in the LPBF process promote the growth of larger dendritic structures

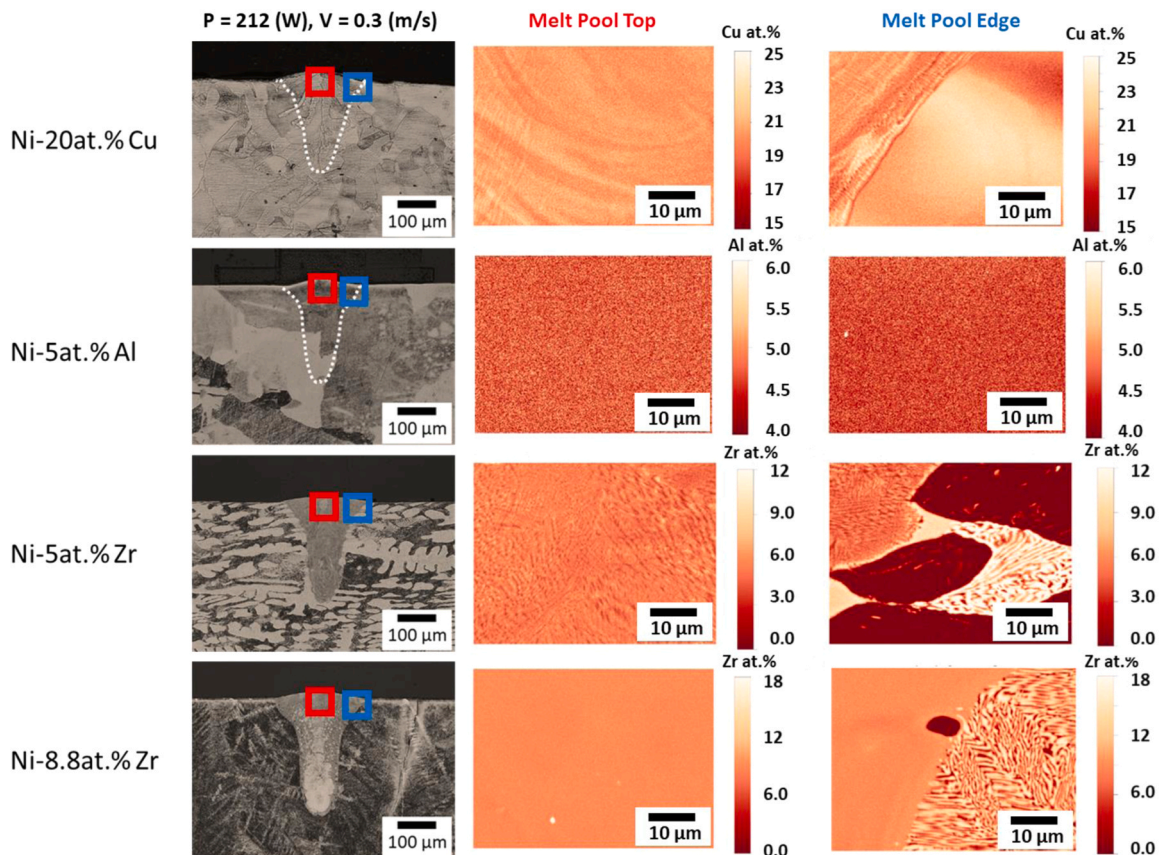
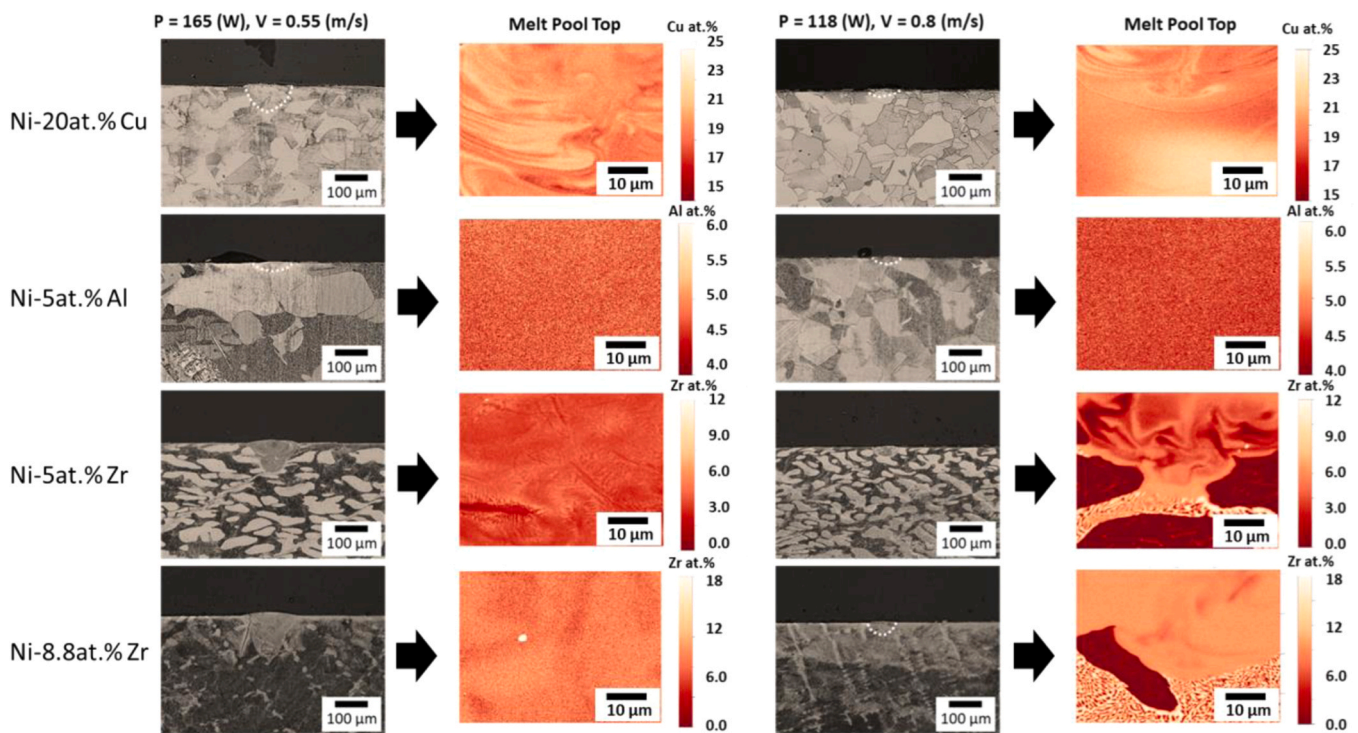


Fig. 8. Optical micrographs of single tracks for each alloying composition printed at 212 W and 0.30 m/s are displayed in the left column with red and blue boxes indicating where WDS maps were conducted. The middle column shows WDS maps taken from the top of each melt pool, and the right column shows maps taken from the edges of each melt pool as color coded in the optical micrographs. White dotted lines indicate the boundaries of single tracks that are difficult to distinguish in these images. (For interpretation of the references to color in this figure legend, the reader is referred to the web version of this article.)



**Fig. 9.** Optical micrographs of single tracks for each alloying composition printed at {165 W and 0.55 m/s} and {118 W and 0.80 m/s} are displayed to the left of their associated WDS maps. All WDS maps were taken from the top of each melt pool. White dotted lines indicate the boundaries of single tracks that are difficult to distinguish in these images.

and vice versa. The heat maps plotted in Fig. 11 show dendrite arm spacing quantified across the parameter space for each material. NiCu is observed to have dendritic structures between laser powers of 70–260 W and scan speed between 0 and 0.7 m/s, whereas dendrites are observed between 70 and 260 W and 0–1.3 m/s in Ni-5Zr. This larger range of dendritic growth in Ni-5Zr can be attributed to the larger solidification range and lower partition coefficient (172 K and 0.11 respectively) compared to NiCu (20 K and 0.74 respectively). However, the differences in scale bars for the two alloys in Fig. 11 indicate that larger PDAS is observed in NiCu compared to Ni-5Zr. The heat maps also indicate that planar growth is observed throughout the parameter space for both NiAl and Ni-8.8Zr. These maps give a qualitative indication of expected dendritic growth throughout the parameter space for each of the alloys.

To validate the PDAS heat maps displayed in Fig. 11, the cubes are printed at three locations in the parameter space based on both the porosity processing maps and PDAS heat maps. Figs. 12–15 display the combined porosity-microstructure processing maps for NiCu, NiAl, Ni-5Zr, and Ni-8.8Zr respectively, as well as WDS maps for each of the printed cubes. Compositional measurements from the as-printed cubes correlate well with expected dendrite growth displayed in each of the processing maps. Cubes selected at PDAS values of 0.7 μm, 0.4 μm, and 0 μm from the NiCu processing map in Fig. 12 demonstrate this correlation, showing significant dendrite structures at the 0.7 μm PDAS parameter set, moderate dendrite structures at 0.4 μm, and a planar microstructure at 0 μm. Solute depletion along melt pool boundaries is observable in each of the NiCu cubes. Similarly, Fig. 14 displays significant segregation of Zr (up to 4 at%) in cubes printed at PDAS values of 0.3 μm and 0.25 μm in the processing map, but shows lower relative amounts of Zr segregation (~1 at%) at 0.15 μm. Both NiAl and Ni-8.8Zr in Figs. 13 and 15 display planar microstructures in cubes across the parameter space, as is expected from the processing maps. Additionally, a general depletion of Al is observed in Fig. 13 with an increase in laser power. This may be due to the evaporation of Al in the as-printed bulk material under higher laser powers. These results validate that observations of microsegregation and dendrite size in single tracks can be

used to qualitatively assess microstructural development in printed parts and generate microstructure processing maps for L-PBF.

### 3.5. Statistical analysis and empirical equation for PDAS in L-PBF

Several equations have been proposed to predict PDAS for alloys subjected to rapid solidification conditions. The Kurz-Fisher [59] and Trivedi [60] models predict PDAS as a function of material properties such as the equilibrium and rapid solidification ranges, liquid diffusion coefficient, Gibbs-Thomson coefficient, and partition coefficient as well as solidification conditions such as the temperature gradient and solidification rate. However, material properties such as the Gibbs-Thomson coefficient and liquid diffusion coefficient are not easily obtainable for new alloy systems. Additionally, L-PBF conditions can vary locally throughout a build and solidification conditions are subject to significant variation depending on the local thermal histories and heat dissipation mechanisms. These variables do not readily translate to usable parameter input data or material selection constraints. A model predicting PDAS as a function of easily obtainable material properties and L-PBF process parameters such as laser power and scan speed would therefore be useful in determining PDAS. Single track data from this study is used to statistically test the sensitivity of PDAS values to material properties and process parameters, and an empirical equation is developed to predict PDAS in L-PBF.

The dataset presented in this study is considered sparse and high dimensional. To better understand the influence of different variables on PDAS, as well as to create predictive models, materials informatics strategies were employed. Materials informatics allows analysis of high-dimensional materials data through machine learning [61,62]. Features included in the database consisted of the material properties listed in Table 2, single track process parameters and PDAS values, and other available thermodynamic properties of the alloy systems. The PDAS dataset collected from the four alloys was initially sampled to obtain an optimal distribution of data representative of the PDAS value range. This required many of the PDAS values equal to zero to be dropped from the

## Ni-20at.% Cu

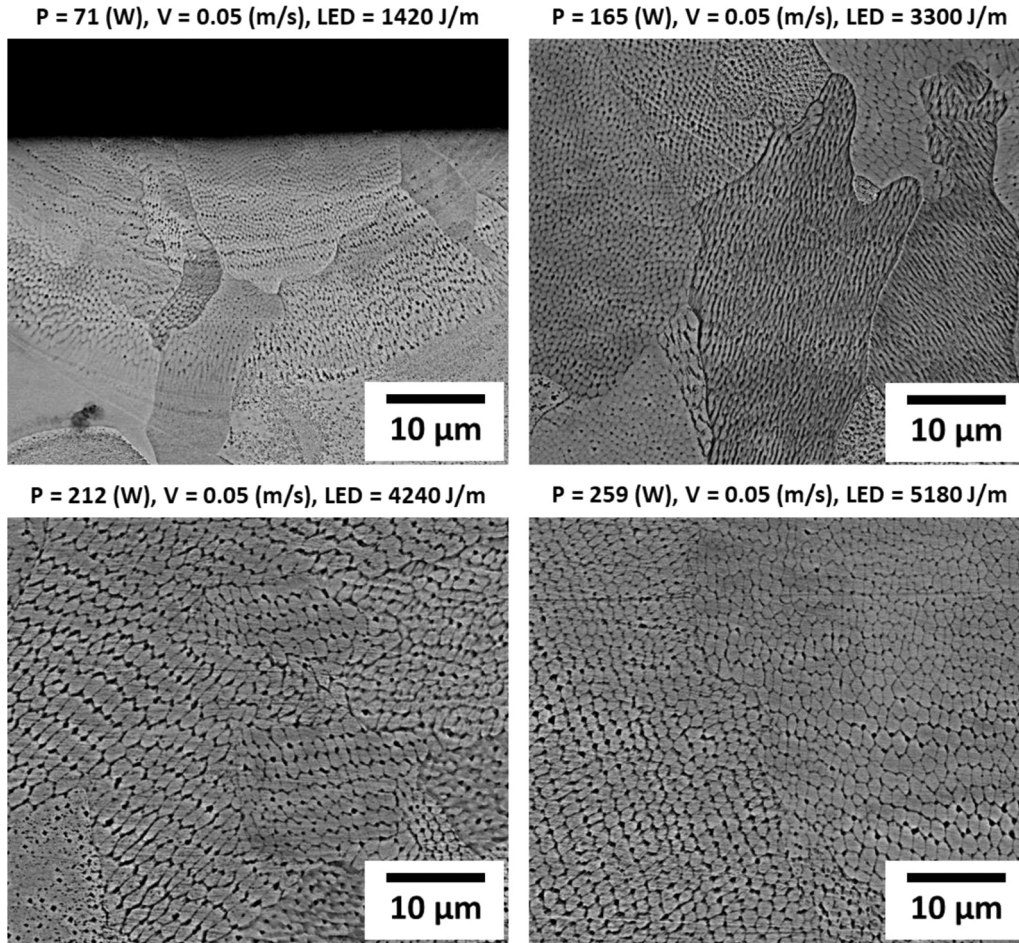


**Fig. 10.** Backscattered electron images taken of Ni-20 at% Cu single tracks printed at {71 W and 0.05 m/s}, {165 W and 0.05 m/s}, {212 W and 0.05 m/s}, and {259 W and 0.05 m/s}. These micrographs display the significant differences in cellular-dendritic segregation structures at different locations in the laser power-scan speed parameter space.

analysis. The dataset was then split into two parts with 80% of the data being used to train the machine learning model and the remaining 20% of the data used to test model accuracy. Primary analysis of the data was done using a Random Forest regression technique [63] and the model performance values for the test set are displayed in Fig. 16a. The trained model predicted the test set with a root mean squared error of 0.12  $\mu\text{m}$  and a mean absolute error of 0.08  $\mu\text{m}$ , indicating a high degree of model accuracy. Feature sensitivity analysis was used to identify feature importance and determined that the most important features contributing to PDAS were: scan speed, melting temperature, laser power, partition coefficient, and freezing range, as can be seen in Fig. 16b. Scan speed is observed to have the most substantial impact on PDAS. Laser scan speed is highly correlated with solidification growth rate since the tail of a molten pool is expected to have a growth rate equal to the scan speed of the laser [14]. This result is therefore consistent with expectations of laser scan speed's effect on dendrite growth. PDAS is also observed to be sensitive to alloy melting temperature. However, this sensitivity may be inflated by the relatively low number of alloy systems used as training data for this analysis as well as the omission of many of the PDAS values equal to zero as previously discussed.

Feature engineering and generation was used to create new features using mathematical operators and combinations of process parameters and material properties. A linear regression model was then used to evaluate the accuracy of the new features in predicting PDAS. Linear

regression is employed for its simplicity and low computational cost. Features that showed poor predictive accuracy were dropped from the model, and those with good performance were improved upon in an iterative process. This feature engineering and selection process is described in more detail by Horn et al. [64]. No more than 6 parameter and material property combinations were used to generate a new feature. After numerous iterations, the following empirical formula was derived:

$$\lambda_{PDAS} = \text{Log}\left(\frac{P^{0.18} \Delta T^{0.26} k_e^{0.75} c_p^5}{v^{0.18} T_m^{9.41}}\right) + 16.10, \quad (2)$$

Here,  $P$  is laser power,  $v$  is laser scan speed,  $\Delta T$  equilibrium solidification range,  $k_e$  is the partition coefficient,  $c_p$  is the specific heat capacity,  $T_m$  is the alloy melting temperature, and  $\lambda_{PDAS}$  is the primary dendrite arm spacing in  $\mu\text{m}$ . This equation is fit to single track PDAS data in Fig. 16c and exhibits a root mean squared error of 0.0842  $\mu\text{m}$  and a mean absolute error of 0.0641  $\mu\text{m}$ . The feature engineered model takes a similar approach to the classical mass balance and minimum undercooling PDAS prediction model developed by Hunt [65] in that  $k_e$  and  $\Delta T$  are multiplied in the expression. This relationship illustrates the differences in segregation across the parameter space between the alloys. If the  $k_e$  and  $\Delta T$  values are multiplied for each alloy, NiCu has a  $k_e \times \Delta T \approx 15$  and Ni-5Zr has a value  $\approx 19$ , whereas NiAl and Ni-8.8Zr have values of  $k_e \times \Delta T$  near or equal to zero. However, this does not explain

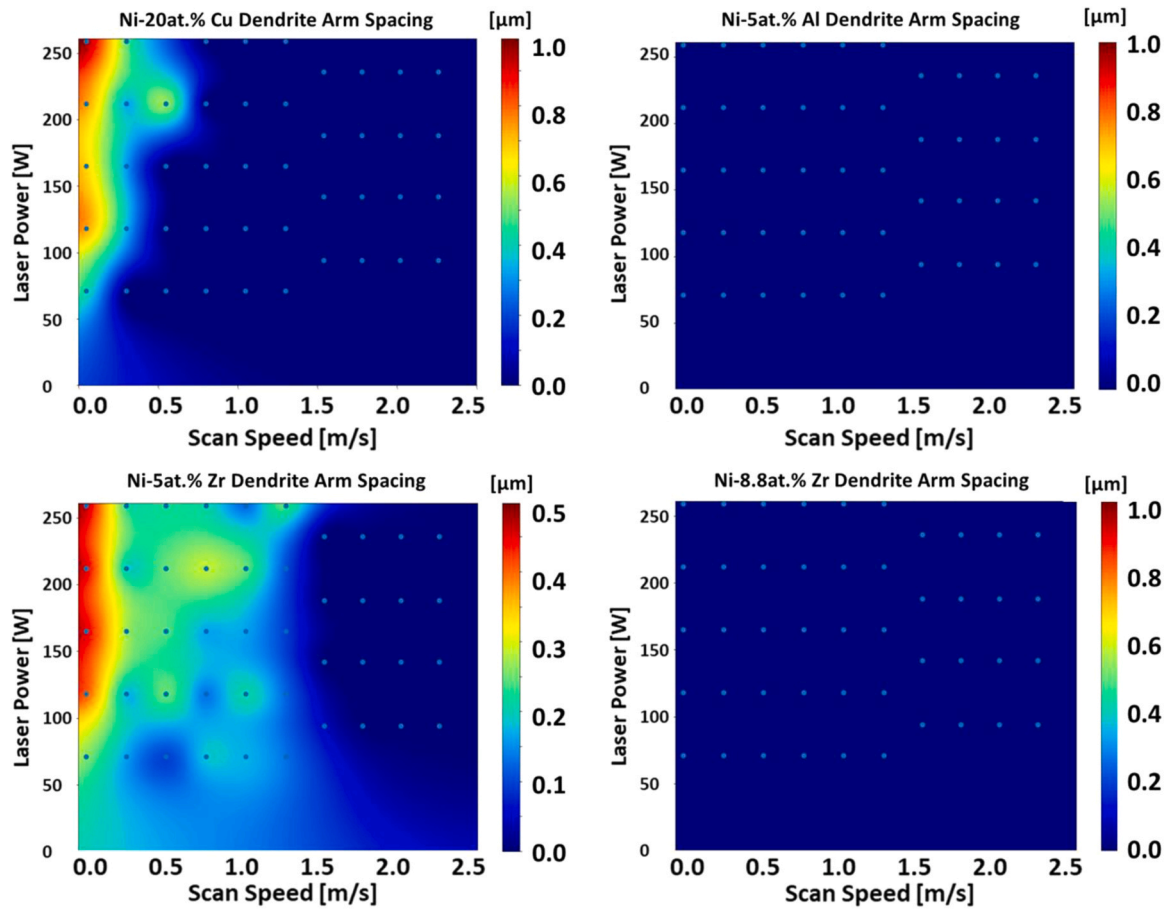


Fig. 11. Primary dendrite arm spacing measurements taken from 46 single tracks across the parameter space are interpolated using multilevel B-splines approximation to construct heat maps of each alloy. Observations of planar growth instead of cellular-dendritic growth structures are indicated by zero values in the heat maps. The markers displayed inside the heat maps indicate the location of 46 single tracks that PDAS measurements were taken from.

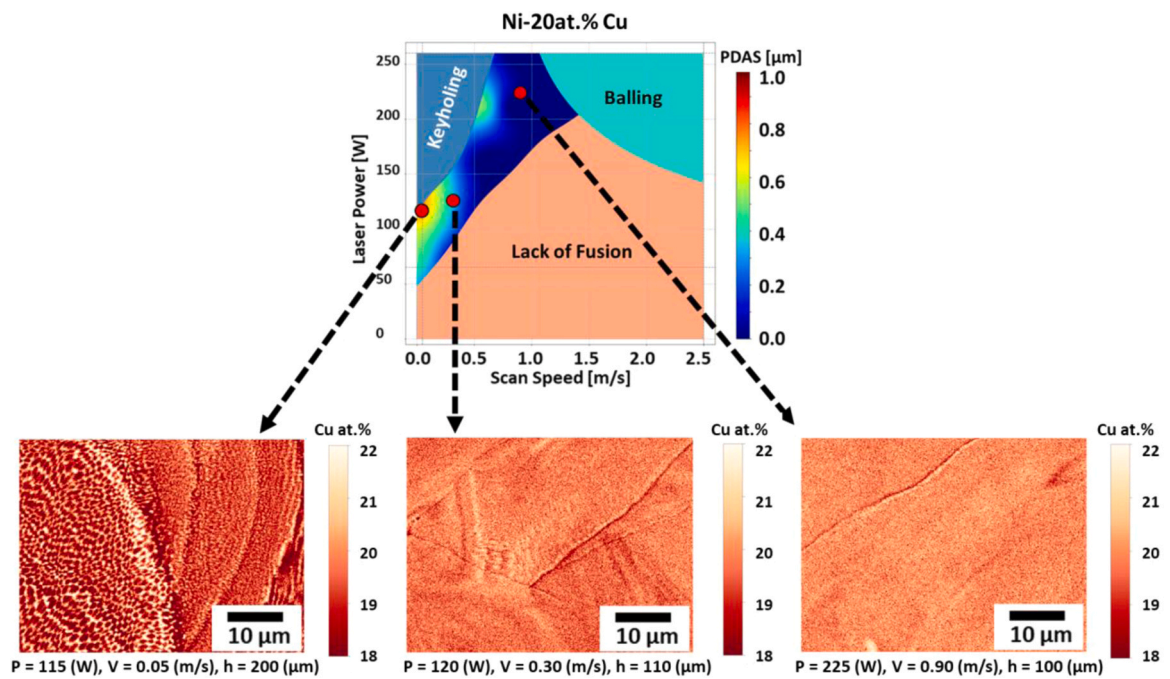


Fig. 12. A combined Porosity-Microstructure processing map for Ni-20 at% Cu, as well as wavelength dispersive spectroscopy (WDS) composition maps taken from each of the printed cubes listed in Table 2. The cubes were printed at  $\{P = 115 \text{ W}, v = 0.05 \text{ m/s}, h = 200 \mu\text{m}\}$ ,  $\{P = 120 \text{ W}, v = 0.30 \text{ m/s}, h = 110 \mu\text{m}\}$ , and  $\{P = 225 \text{ W}, v = 0.90 \text{ m/s}, h = 100 \mu\text{m}\}$ .

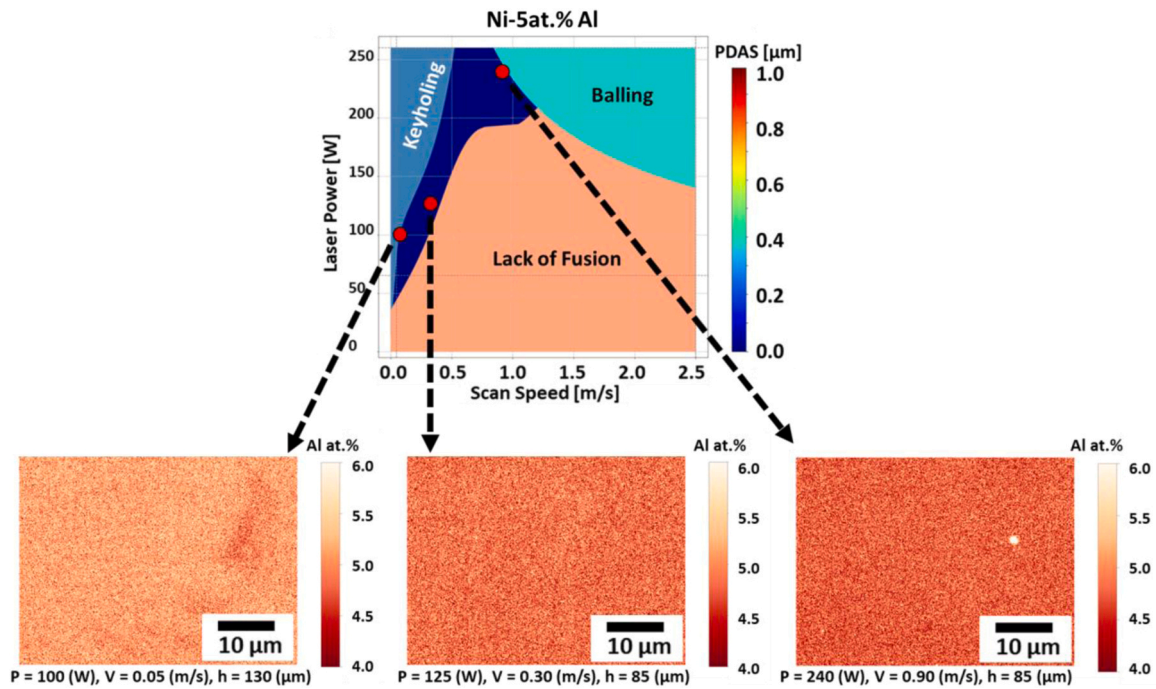


Fig. 13. A combined Porosity-Microstructure processing map for Ni-5 at% Al, as well as wavelength dispersive spectroscopy (WDS) composition maps taken from each of the printed cubes listed in Table 2. The cubes were printed at  $\{P = 100 \text{ W}, v = 0.05 \text{ m/s}, h = 130 \text{ }\mu\text{m}\}$ ,  $\{P = 125 \text{ W}, v = 0.30 \text{ m/s}, h = 85 \text{ }\mu\text{m}\}$ , and  $\{P = 240 \text{ W}, v = 0.90 \text{ m/s}, h = 85 \text{ }\mu\text{m}\}$ .

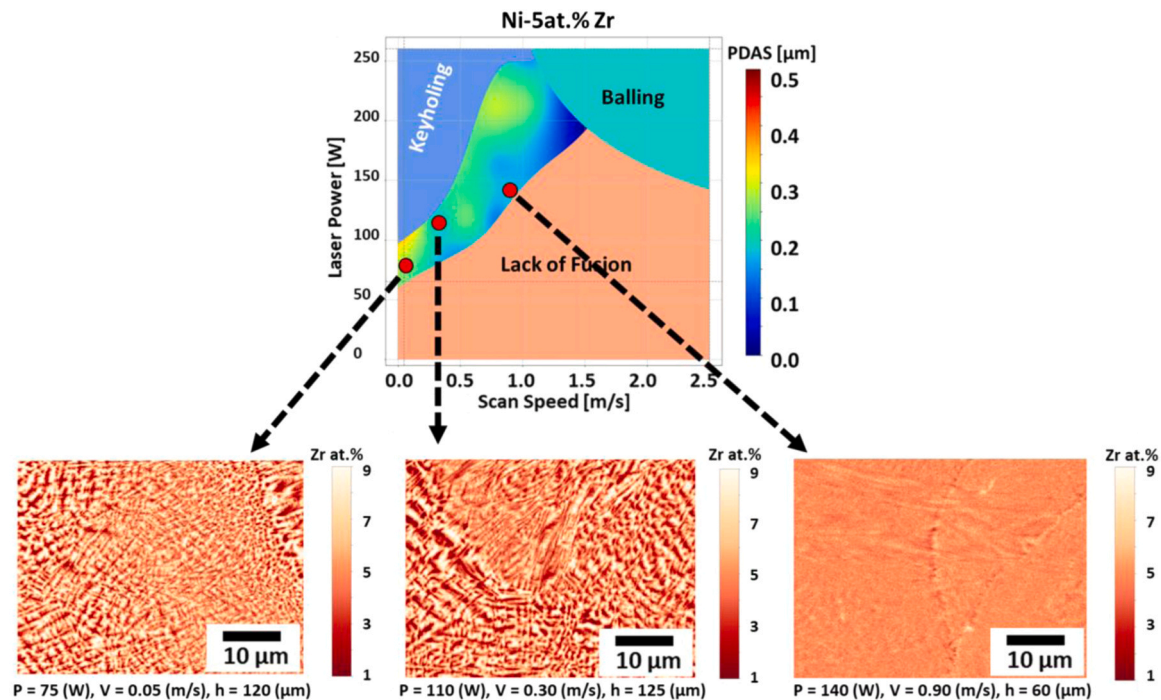


Fig. 14. A combined Porosity-Microstructure processing map for Ni-5 at% Zr, as well as wavelength dispersive spectroscopy (WDS) composition maps taken from each of the printed cubes listed in Table 2. The cubes were printed at  $\{P = 75 \text{ W}, v = 0.05 \text{ m/s}, h = 120 \text{ }\mu\text{m}\}$ ,  $\{P = 110 \text{ W}, v = 0.30 \text{ m/s}, h = 125 \text{ }\mu\text{m}\}$ , and  $\{P = 140 \text{ W}, v = 0.90 \text{ m/s}, h = 60 \text{ }\mu\text{m}\}$ .

why the NiCu single tracks were observed to have PDAS values larger than Ni-5Zr. Thermal properties not reported for these alloy systems such as the liquid diffusion coefficients, Gibbs-Thomson coefficients, and thermal conductivities may play a role in the observed differences in absolute PDAS values. Additionally, the inverse relationship between  $k_e$  and  $\Delta T$  and their effect on dendrite growth may explain why PDAS does

not appear to be as sensitive to these values as  $v$  and  $P$ . In general, a larger solidification range implies a smaller partition coefficient. When the quantities are multiplied this inverse relationship results in them ‘canceling’ each other. In contrast, the other important factors ( $T_m$ ,  $P$ , and  $v$ ) are completely independent of each other and their effect on PDAS is more direct. Due to the limited dataset generated by this study it

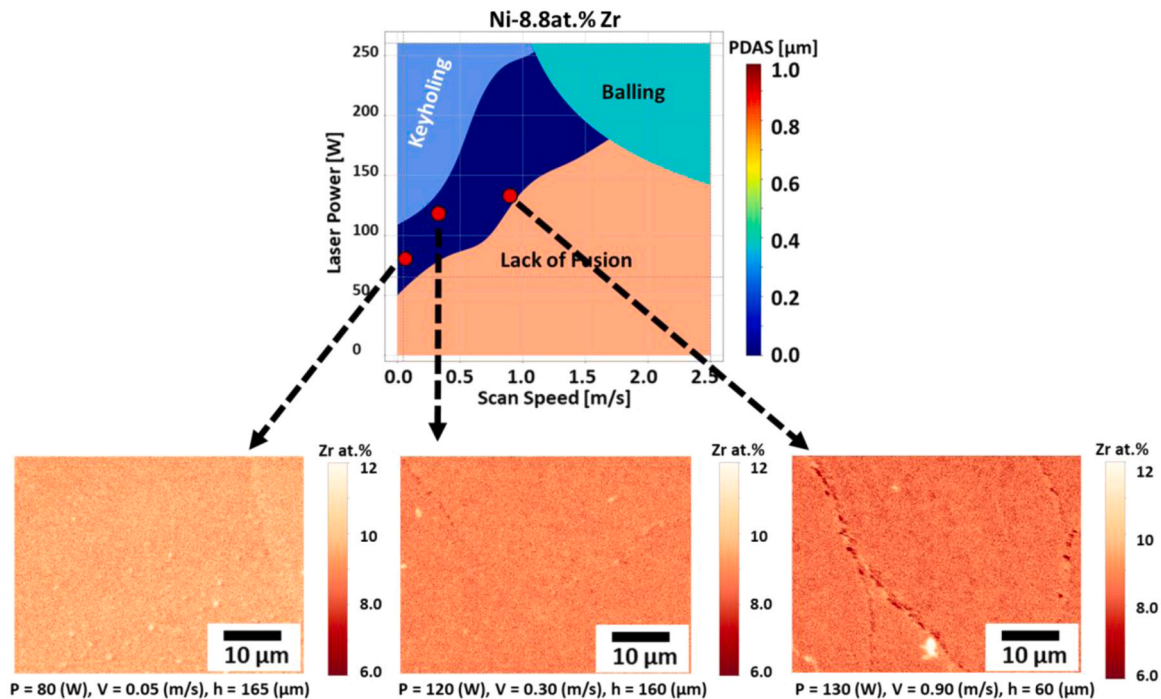


Fig. 15. A combined Porosity-Microstructure processing map for Ni-8.8 at% Zr, as well as wavelength dispersive spectroscopy (WDS) composition maps taken from each of the printed cubes listed in Table 2. The cubes were printed at  $\{P = 80 \text{ W}, v = 0.05 \text{ m/s}, h = 165 \mu\text{m}\}$ ,  $\{P = 120 \text{ W}, v = 0.30 \text{ m/s}, h = 160 \mu\text{m}\}$ , and  $\{P = 130 \text{ W}, v = 0.90 \text{ m/s}, h = 60 \mu\text{m}\}$ .

is likely that the empirical model will need modification to be generalizable for significantly different alloy systems. However, a generalizable model using L-PBF process parameters and simple material property inputs will likely prove invaluable for designing new alloys for AM.

#### 4. Summary and conclusions

The present work reports the effects of alloying composition, phase diagram features, and material properties on the printability and solidification microstructures in four binary nickel-based alloys, namely, Ni-20 at% Cu, Ni-5 at% Al, Ni-5 at% Zr, and Ni-8.8 at% Zr. A methodology for developing porosity-microstructure processing maps across the laser power – scan speed parameter space is established and validated for each of these alloys to determine how alloy composition and material properties affect printability and microstructure in L-PBF. The following conclusions can be drawn from this study:

- Alloy melting temperature is observed to have a significant effect on both melt pool dimensions and printability in L-PBF. Alloys with high melting temperatures require more energy to melt, resulting in shallower melt pool structures. These shallow melt pools result in larger lack of fusion boundaries in the processing maps developed in this study, shrinking the parameter space expected to produce porosity free parts. However, keyhole defect boundaries in these processing maps are oppositely affected by melting temperature. Larger keyhole defect regions are observed in alloys with lower melting temperatures. The lack of fusion boundary is more sensitive to this phenomenon than the keyhole boundary, resulting in larger optimal parameter ranges for alloys with lower melting temperatures.
- Solidification temperature range and partition coefficient have a substantial impact on microsegregation in L-PBF. A wider region of the L-PBF parameter space is expected to result in segregation in alloys with large solidification ranges and small partition coefficients. Dendrite size and segregation amount are also highly dependent on scan speed and, to a lesser extent, laser power. Larger

dendrites with increased solute segregation form when using low scan speeds and high laser powers.

- Quantification of primary dendrite arm spacing (PDAS) in single track scans across the parameter space allowed for the construction of processing maps qualitatively detailing expected segregation across the parameter space. These processing maps were successful at predicting the extent of solute segregation as demonstrated in four Ni-based alloys. Control over microsegregation can be achieved by optimizing process parameters utilizing these processing maps.
- An empirical equation to predict PDAS using L-PBF process parameters and simple material properties was proposed in this study. This model fit well to the measured single track PDAS data. However, the model will likely need modification before it can be generalized to alloys significantly different from those presented here.
- The methodology introduced in this study allows for the successful development of processing maps capable of predicting both porosity formation (and thus the elimination of porosity) and microsegregation in bulk parts built using L-PBF. In addition to easing process parameter optimization for new alloy systems, this methodology also provides a pathway to evaluate and compare printability across alloy systems.

#### CRediT authorship contribution statement

R.S. and I.K. contributed to the conceptualization of the experiments and experimental methodology. R.S. Contributed to paper writing and revisions, preparation of the material, and conducting all characterization experiments. J.Y. Contributed to fabricating the additively manufactured material used for experiments, E-T modeling and SVM classification for the printability maps, and interpolation of the microsegregation data for microstructure processing maps, and plotting of all processing maps used in the study. A.W. Contributed to optical micrograph characterization of the material, extracting measurements from characterization experiments, and data analysis. W.T. Contributed to the random forest machine learning model analysis of microsegregation data, feature engineering to develop the empirical microsegregation

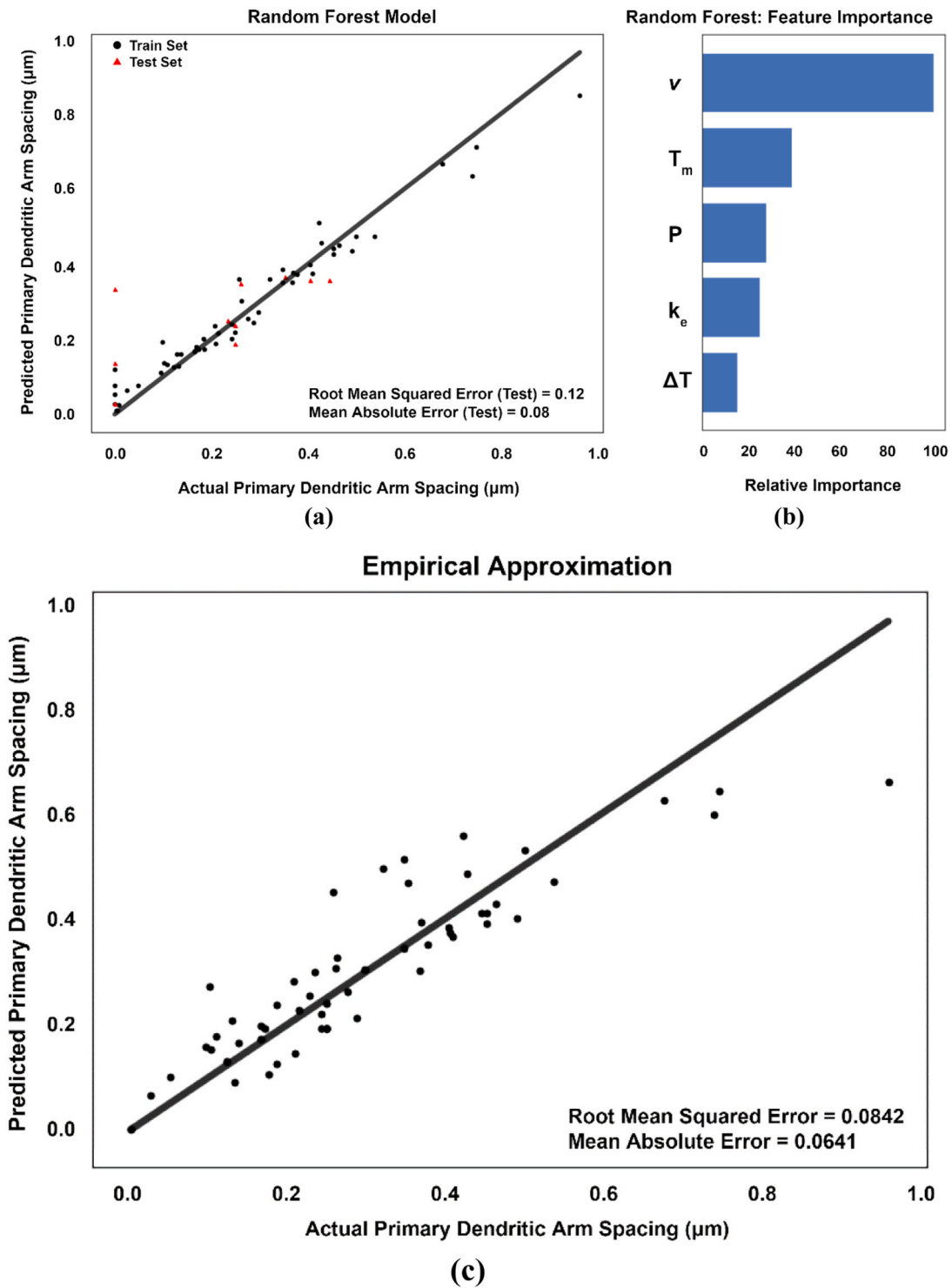


**Fig. 16.** Materials informatics strategies employed to analyze the high-dimensional materials data presented in this study through machine learning. a) A Random Forest validation plot showing the model fit to the train and test PDAS datasets. b) A Random Forest feature importance plot displaying the sensitivity of PDAS to material properties and process parameters. c) A validation plot displaying the predictive accuracy of the empirical model developed in this study.  $v$ : Laser Scan Speed,  $T_m$ : Alloy Melting Temperature,  $P$ : Laser Power,  $k_e$ : Partition Coefficient,  $\Delta T$ : Alloy Solidification Temperature Range.

formula, and paper writing on these topics. A.E., R.A., and I.K. Co-supervised the scholarly work, and secured all resources needed to conduct the work. All coauthors reviewed the manuscript.

**Declaration of Competing Interest**

The authors declare the following financial interests/personal

relationships which may be considered as potential competing interests: Ibrahim Karaman reports financial support was provided by US Army Research Office. Raymundo Arroyave reports financial support was provided by US Army Research Office. Alaa Elwany reports financial support was provided by US Army Research Office. Ibrahim Karaman has patent pending to Texas A&M Engineering Experiment Station. Alaa Elwany has patent pending to Texas A&M Engineering Experiment

Station. Raymundo Arroyave has patent pending to Texas A&M Engineering Experiment Station. Raiyan Seede has patent pending to Texas A&M Engineering Experiment Station.

### Data availability

The data that support the findings of this study are available from the corresponding author, [IK], upon reasonable request.

### Acknowledgments

The present work was carried out with the support from the Army Research Office (ARO), USA under Contract No. W911NF-18-1-0278. Authors Alaa Elwany and Jiahui Ye also acknowledge support from the National Science Foundation (NSF), USA through Grant No. 1846676. The authors would like to acknowledge Dr. Andrew Mott for his support in operating the Cameca SXFive Microprobe and Bing Zhang for her contribution to operation of the 3D Systems ProX DMP 200.

### References

- [1] K.N. Amato, S.M. Gaytan, L.E. Murr, E. Martinez, P.W. Shindo, J. Hernandez, S. Collins, F. Medina, Microstructures and mechanical behavior of Inconel 718 fabricated by selective laser melting, *Acta Mater.* 60 (2012) 2229–2239.
- [2] T. DebRoy, H.L. Wei, J.S. Zuback, T. Mukherjee, J.W. Elmer, J.O. Milewski, A. M. Beese, A. Wilson-Heid, A. De, W. Zhang, Additive manufacturing of metallic components – process, structure and properties, *Prog. Mater. Sci.* 92 (2018) 112–224.
- [3] Z. Wang, K. Guan, M. Gao, X. Li, X. Chen, X. Zeng, The microstructure and mechanical properties of deposited-IN718 by selective laser melting, *J. Alloy. Compd.* 513 (2012) 518–523.
- [4] W.M. Tucho, P. Cuvillier, A. Sjolyst-Kverneland, V. Hansen, Microstructure and hardness studies of Inconel 718 manufactured by selective laser melting before and after solution heat treatment, *Mater. Sci. Eng. A* 689 (2017) 220–232.
- [5] R. Seede, A. Mostafa, V. Brailovski, M. Jahazi, M. Medraj, Microstructural and microhardness evolution from homogenization and hot isostatic pressing on selective laser melted Inconel 718: structure, texture, and phases, *JMMP 2* (2018) 30.
- [6] K. Kempen, L. Thijs, J. Van Humbeeck, J.P. Kruth, Mechanical properties of AlSi10Mg produced by selective laser melting, *Phys. Procedia* 39 (2012) 439–446.
- [7] N. Read, W. Wang, K. Essa, M.M. Attallah, Selective laser melting of AlSi10Mg alloy: process optimisation and mechanical properties development, *Mater. Des.* 65 (2015) 417–424.
- [8] E. Liverani, S. Toschi, L. Ceschini, A. Fortunato, Effect of selective laser melting (SLM) process parameters on microstructure and mechanical properties of 316L austenitic stainless steel, *J. Mater. Process. Technol.* 249 (2017) 255–263.
- [9] D. Agius, K. Kourousis, C. Wallbrink, A review of the as-built SLM Ti-6Al-4V mechanical properties towards achieving fatigue resistant designs, *Metals* 8 (2018) 75.
- [10] Y. Wang, C. Kamath, T. Voisin, Z. Li, A processing diagram for high-density Ti-6Al-4V by selective laser melting, *Rapid Prototyp. J.* 24 (2018) 1469–1478.
- [11] H. Zhang, H. Zhu, T. Qi, Z. Hu, X. Zeng, Selective laser melting of high strength Al-Cu-Mg alloys: processing, microstructure and mechanical properties, *Mater. Sci. Eng. A* 656 (2016) 47–54.
- [12] W. Xiong, L. Hao, Y. Li, D. Tang, Q. Cui, Z. Feng, C. Yan, Effect of selective laser melting parameters on morphology, microstructure, densification and mechanical properties of supersaturated silver alloy, *Mater. Des.* 170 (2019), 107697.
- [13] A. Iveković, N. Omidvari, B. Vrancken, K. Lietaert, L. Thijs, K. Vanmeensel, J. Vleugels, J.P. Kruth, Selective laser melting of tungsten and tungsten alloys, *Int. J. Refract. Met. Hard Mater.* 72 (2018) 27–32.
- [14] K. Karayagiz, L. Johnson, R. Seede, V. Attari, B. Zhang, X. Huang, S. Ghosh, T. Duong, I. Karaman, A. Elwany, R. Arroyave, Finite interface dissipation phase field modeling of Ni-Nb under additive manufacturing conditions, *Acta Mater.* 185 (2020) 320–339.
- [15] A. Mostafa, I.P. Rubio, V. Brailovski, M. Jahazi, M. Medraj, Structure, texture and phases in 3D printed IN718 alloy subjected to homogenization and HIP treatments, in: *Metals*, 7, 2017, p. 196.
- [16] T. Antonsson, H. Fredriksson, The effect of cooling rate on the solidification of INCONEL 718, *Metall. Mater. Trans. B-Process. Metall. Mater. Process. Sci.* 36 (2005) 85–96.
- [17] X. Wu, J. Liang, J. Mei, C. Mitchell, P.S. Goodwin, W. Voice, Microstructures of laser-deposited Ti-6Al-4V, *Mater. Des.* 25 (2004) 137–144.
- [18] V.A. Popovich, E.V. Borisov, V.S. Sufiyarov, A.A. Popovich, Tailoring the properties in functionally graded alloy Inconel 718 using additive technologies, *Met. Sci. Heat. Treat.* 60 (2019) 701–709.
- [19] H. Qi, M. Azer, A. Ritter, Studies of standard heat treatment effects on microstructure and mechanical properties of laser net shape manufactured INCONEL 718, *Metall. Mater. Trans. A Phys. Metall. Mater. Sci.* 40 (2009) 2410–2422.
- [20] T. Wang, Y.Y. Zhu, S.Q. Zhang, H.B. Tang, H.M. Wang, Grain morphology evolution behavior of titanium alloy components during laser melting deposition additive manufacturing, *J. Alloy. Compd.* 632 (2015) 505–513.
- [21] Y.-J. Liang, X. Cheng, H.-M. Wang, A new microsegregation model for rapid solidification multicomponent alloys and its application to single-crystal nickel-base superalloys of laser rapid directional solidification, *Acta Mater.* 118 (2016) 17–27.
- [22] P. Mohammadpour, A. Plotkowski, A.B. Phillion, Revisiting solidification microstructure selection maps in the frame of additive manufacturing, *Addit. Manuf.* 31 (2020), 100936.
- [23] T. Mukherjee, H.L. Wei, A. De, T. DebRoy, Heat and fluid flow in additive manufacturing—Part II: powder bed fusion of stainless steel, and titanium, nickel and aluminum base alloys, *Comput. Mater. Sci.* 150 (2018) 369–380.
- [24] T. Mukherjee, V. Manvatkar, A. De, T. DebRoy, Dimensionless numbers in additive manufacturing, *J. Appl. Phys.* 121 (2017), 064904.
- [25] T. Mukherjee, T. Debroy, Mitigation of lack of fusion defects in powder bed fusion additive manufacturing, *J. Manuf. Process.* 36 (2018) 442–449.
- [26] L. Johnson, M. Mahmoudi, B. Zhang, R. Seede, J.T. Maier, H.J. Maier, I. Karaman, A. Elwany, Assessing printability maps in additive manufacturing of metal alloys, *Acta Mater.* 176 (2019) 199–210.
- [27] R. Seede, D. Shoukr, B. Zhang, A. Whitt, S. Gibbons, P. Flater, A. Elwany, R. Arroyave, I. Karaman, An ultra-high strength martensitic steel fabricated using selective laser melting additive manufacturing: densification, microstructure, and mechanical properties, *Acta Mater.* 186 (2020) 199–214.
- [28] R. Rashid, S.H. Masood, D. Ruan, S. Palanisamy, R.A. Rahman Rashid, M. Brandt, Effect of scan strategy on density and metallurgical properties of 17-4PH parts printed by Selective Laser Melting (SLM), *J. Mater. Process. Technol.* 248 (2017) 502–511.
- [29] G. Kasperovich, J. Haubrich, J. Gussone, G. Requena, Correlation between porosity and processing parameters in TiAl6V4 produced by selective laser melting, *Mater. Des.* 105 (2016) 160–170.
- [30] J. Delgado, J. Ciurana, C.A. Rodríguez, Influence of process parameters on part quality and mechanical properties for DMLS and SLM with iron-based material, *Int. J. Adv. Manuf. Technol.* 60 (2012) 601–610.
- [31] R. Rashid, S.H. Masood, D. Ruan, S. Palanisamy, R.A. Rahman Rashid, J. Elambasseril, M. Brandt, Effect of energy per layer on the anisotropy of selective laser melted AlSi12 aluminium alloy, *Addit. Manuf.* 22 (2018) 426–439.
- [32] M. Letenneur, A. Kreitzberg, V. Brailovski, Optimization of laser powder bed fusion processing using a combination of melt pool modeling and design of experiment approaches: density control, *JMMP 3* (2019) 21.
- [33] C. Kamath, B. El-dasher, G.F. Gallegos, W.E. King, A. Sisto, Density of additively-manufactured, 316L SS parts using laser powder-bed fusion at powers up to 400W, *Int. J. Adv. Manuf. Technol.* 74 (2014) 65–78.
- [34] A. Foroozmehr, M. Badrossamay, E. Foroozmehr, S. Golabi, Finite element simulation of selective laser melting process considering optical penetration depth of laser in powder bed, *Mater. Des.* 89 (2016) 255–263.
- [35] B. Zhang, R. Seede, L. Xue, K.C. Atli, C. Zhang, A. Whitt, I. Karaman, R. Arroyave, A. Elwany, An efficient framework for printability assessment in laser powder bed fusion metal additive manufacturing, *Addit. Manuf.* (2021), 102018.
- [36] A. Pfaff, M. Jäcklein, M. Schlager, W. Harwick, K. Hoschke, F. Balle, An empirical approach for the development of process parameters for laser powder bed fusion, *Materials* (2020) 5400.
- [37] J.N. Zhu, E. Borisov, X. Liang, E. Farber, V.A. Hermans, M.J.M. Popovich, Predictive analytical modelling and experimental validation of processing maps in additive manufacturing of nitinol alloys, *Addit. Manuf.* 38 (2021), 101802.
- [38] L. Xue, K.C. Atli, S. Picak, C. Zhang, B. Zhang, A. Elwany, R. Arroyave, I. Karaman, Controlling martensitic transformation characteristics in defect-free NiTi shape memory alloys fabricated using laser powder bed fusion and a process optimization framework, *Acta Mater.* 215 (2021), 117017.
- [39] P. Konda Gokuldoss, Design of next-generation alloys for additive manufacturing, *Mater. Des. Process. Commun.* 1 (2019).
- [40] J.N. DuPont, J.C. Lippold, S.D. Kiser, *Welding Metallurgy and Weldability of Nickel Based Alloys*, 2000 doi: <https://doi.org/10.1002/cbdu.200490137/abstract>.
- [41] K.A. Jackson, K.M. Beatty, K.A. Gudge, An analytical model for non-equilibrium segregation during crystallization, *J. Cryst. Growth* 271 (2004) 481–494.
- [42] J. Das, K. Kim, F. Baier, W. Löser, J. Eckert, High-strength Ti-base ultrafine eutectic with enhanced ductility, *Appl. Phys. Lett.* 87 (2005), 161907.
- [43] C. Tiwary, D. Roy Mahapatra, K. Chattopadhyay, Effect of length scale on mechanical properties of Al-Cu eutectic alloy, *Appl. Phys. Lett.* 101 (2012), 171901.
- [44] J. Miettinen, Ni-Cu Phase Diagram, ASM Alloy Phase Diagrams Database, ASM International, Materials Park, OH, 2016 doi: <http://www.asminternational.org.srv-proxy2.library.tamu.edu>.
- [45] J. Miettinen, Ni-Al Phase Diagram, ASM Alloy Phase Diagrams Database, ASM International, Materials Park, OH, 2016 doi: <http://www.asminternational.org.srv-proxy2.library.tamu.edu>.
- [46] N. Wang, C. Li, Z. Du, F. Wang, Ni-Zr Phase Diagram, ASM Alloy Phase Diagrams Database, ASM International, Materials Park, OH, 2016 doi: <http://www.asminternational.org.srv-proxy2.library.tamu.edu>.
- [47] J.-O. Andersson, T. Helander, L. Höglund, P. Shi, B. Sundman, Thermo-Calc and DICTRA, computational tools for materials science, *Calphad* 26 (2002) 273–312.
- [48] C. Yang, J. Gao, Y. Zhang, M. Kolbe, D.M. Herlach, New evidence for the dual origin of anomalous eutectic structures in undercooled Ni-Sn alloys: in situ observations and EBSD characterization, *Acta Mater.* 59 (2011) 3915–3926.

- [49] C. Clopet, R. Cochrane, A. Mullis, Spasmodic growth during the rapid solidification of undercooled Ag-Cu eutectic melts, *Appl. Phys. Lett.* 102 (2013), 031906.
- [50] T.W. Eagar, N.-S. Tsai, Temperature fields produced by traveling distributed heat sources, *Weld. J.* 62 (1983) 346–355.
- [51] H. Gong, H. Gu, K. Zeng, J. Dilip, D. Pal, B. Stucker, J.J. Lewandowski, Melt pool characterization for selective laser melting of Ti-6Al-4V pre-alloyed powder, *Solid Free. Fabr. Symp.* (2014).
- [52] R. Rai, J.W. Elmer, T.A. Palmer, T. Debroy, Heat transfer and fluid flow during keyhole mode laser welding of tantalum, Ti-6Al-4V, 304L stainless steel and vanadium, *J. Phys. D Appl. Phys.* 40 (2007) 5753–5766.
- [53] M.C. Kennedy, A. O'Hagan, Bayesian calibration of computer models, *J. R. Stat. Soc. Ser. B (Stat. Methodol.)* 63 (2001) 425–464.
- [54] J.D. Roehling, A. Perron, J.L. Fattebert, T. Haxhimali, G. Guss, T.T. Li, D. Bober, A. W. Stokes, A.J. Clarke, P.E.A. Turchi, M.J. Matthews, J.T. McKeown, Rapid solidification in bulk Ti-Nb alloys by single-track laser melting, *JOM* 70 (2018) 1589–1597.
- [55] M. Letenneur, V. Brailovski, A. Kreitzberg, V. Paserin, I. Bailon-Poujol, Laser powder bed fusion of water-atomized iron-based powders: process optimization, *JMMP* 1 (2017) 23.
- [56] J.A.K. Suykens, J. Vandewalle, Least squares support vector machine classifiers, *Neural Process. Lett.* 9 (1999) 293–300.
- [57] B. Scholkopf, A.J. Smola, *Learning with Kernels: Support Vector Machines, Regularization, MIT Press*, 2001.
- [58] S. Lee, G. Wolberg, S.Y. Shin, Scattered data interpolation with multilevel B-splines, *IEEE Trans. Vis. Comput. Graph.* 3 (1997) 229–244.
- [59] W. Kurz, D.J. Fisher, Dendrite growth at the limit of stability: tip radius and spacing, *Acta Met.* 29 (1981) 11–20.
- [60] R. Trivedi, Interdendritic spacing: Part II. A comparison of theory and experiment, *Metall. Mater. Trans. A* 15 (1984) 977–982.
- [61] Y. Liu, T. Zhao, W. Ju, S. Shi, Materials discovery and design using machine learning, *J. Mater.* 3 (2017) 159–177.
- [62] Y. Liu, J. Wu, G. Yang, T. Zhao, S. Shi, Predicting the onset temperature ( $T_g$ ) of GexSe1-x glass transition: a feature selection based two-stage support vector regression method, *Sci. Bull.* 64 (2019) 1195–1203.
- [63] V. Svetnik, A. Liaw, C. Tong, J.C. Culberson, R.P. Sheridan, B.P. Feuston, Random forest: a classification and regression tool for compound classification and QSAR modeling, *J. Chem. Inf. Comput. Sci.* 43 (2003) 1947–1958.
- [64] F. Horn, R. Pack, M. Rieger, The autofeat python library for automated feature engineering and selection 1901 (2019). *ArXiv. arXiv*.
- [65] Hunt, J.D., 1977. Cellular and primary dendrite spacings. In: *Solidif. Cast. Met.*, pp. 3–9.